THESIS FOR THE DEGREE OF LICENTIATE OF ENGINEERING

Hydrogen embrittlement and corrosion behavior of low-temperature carburized austenitic stainless steel

XIAO QIN

Department of Industrial and Materials Science

CHALMERS UNIVERSITY OF TECHNOLOGY

Gothenburg, Sweden 2023

Hydrogen embrittlement and corrosion behavior of low-temperature carburized austenitic stainless steel

XIAO QIN

Technical report on IMS-2023-12

Licentiate Thesis at Chalmers University of Technology

Department of Industrial and Materials Science

Chalmers University of Technology

SE-412 96 Gothenburg

Sweden

Telephone + 46 (0)31-772 1000

Printed by Chalmers Reproservice

Gothenburg, Sweden 2023

Hydrogen embrittlement and corrosion behavior of low-temperature carburized austenitic stainless steel

Xiao Qin

Department of Industrial and Materials Science

Chalmers University of Technology

Abstract

For metallic components used in hydrogen environments, hydrogen embrittlement and corrosion have always been important considering potential failure risks. Among many metallic materials, austenitic stainless steel has found broad application because of its excellent corrosion and hydrogen embrittlement resistance. Type AISI304 austenitic stainless steel is promising due to its low cost compared to high alloyed ones, such as 316 and 904 etc. However, 304 is a metastable austenite stainless steel, which is susceptible to strain-induced martensitic transformation. This may reduce corrosion and hydrogen embrittlement resistance in hydrogen-containing environments. Moreover, low hardness and poor fatigue properties also limit their application. It is therefore of great importance to improve hydrogen embrittlement and corrosion resistance of austenitic stainless steel 304.

In recent years, extensive studies have been done to improve the hydrogen embrittlement and corrosion resistance of austenitic stainless steels, such as composition design, processing technology and surface engineering. Low-temperature carburizing (LTC), a surface engineering approach, has great potential because of its economic benefit and sustainability. This treatment can introduce interstitial carbon into the surface region of the steel and form precipitate-free supersaturated solid solution, greatly improving the surface hardness and fatigue properties without compromising the corrosion resistance. It is of great interest to evaluate the feasibility of LTC on the alleviation of hydrogen embrittlement and corrosion for commercial austenitic stainless steel 304 after hydrogen uptake.

In the present study, industrial low-temperature carburizing was performed on commercial AISI304 stainless steel in two conditions (cold worked and solution annealed). Mechanical properties, corrosion behavior, and microstructure of the S phase after hydrogen uptake have been studied and linked. It was found that low-temperature carburizing introduced ~ 22 μm thick S-phase with ultra-high hardness (775 HV) and high surface carbon concentration (2.2 wt.% in solution condition). Hydrogen uptake caused reduced corrosion resistance and hydrogen embrittlement due to hydrogen-induced cracking and hydrogen-induced martensite. For cold-worked 304, hydrogen-induced cracking and martensitic transformation resulted in high susceptibility to hydrogen embrittlement. Solution-annealed 304 showed low hydrogen embrittlement susceptibility due to the austenitic phase with less defects. Low-temperature carburizing improved the hydrogen embrittlement resistance due to the carbon-stabilized austenite. However, the high carbon concentration on the surface of the solution annealed 304 with LTC treatment led to hydrogen-induced cracking and reduced ductility. Potentiodynamic polarization curves and corrosion morphology/chemical analysis revealed that low-temperature carburizing improved corrosion resistance due to high carbon content and stabilized austenite.

Keywords: Austenitic stainless steel, low-temperature carburising, expanded austenite, microstructure, corrosion behavior, hydrogen embrittlement

Preface

This licentiate thesis is based on the work performed at the Department of Industrial and Materials Science at Chalmers University of Technology between December 2021 and December 2023. The work has been carried out under the supervision of Professor Yu Cao (supervisor), Professor Huiqun Liu (co-supervisor) and Professor Lars Nyborg (examiner). This work was financially supported by the Swedish Innovation Agency (2021-01908), the Swedish Energy Agency (2021-036176), the Production Area of Advance and Chalmers University of Technology.

List of Appended Papers

Paper I: Effect of low temperature carburizing on the corrosion and mechanical behavior of AISI 304 austenitic stainless steel after hydrogen charging

X. Qin, A. Bauer, L. Nyborg, E. Tam, H. Liu, Y. Cao

Conference Proceedings of ECHT 2023, Genova, Italy.

Paper II: Effect of low-temperature carburizing on hydrogen embrittlement of AISI 304 austenitic stainless steel

X. Qin, L. Nyborg, H. Liu, A. Bauer, Y. Cao

Manuscript, to be submitted.

Paper III: Corrosion behavior of low-temperature carburized AISI 304 austenitic stainless steel with hydrogen uptake

X. Qin, L. Nyborg, H. Liu, Y. Cao

Manuscript

Papers not included in this thesis

Paper I: Recrystallization and texture evolution of warm-pilgered FeCrAl alloy tube during annealing at 850 °C.

X. Qin, Z. Liu, H. Liu, R. Zhang, Q. Pan, Y. Wang, J. Pei

Journal of Nuclear Materials, 562 (2022), 153575.

Paper II: Recrystallization and texture evolution of cold pilgered FeCrAl cladding tube during annealing at 700 °C~ 1000 °C.

X. Qin, R. Zhang, P. Du, J. Pei, Q. Pan, Y. Cao, H. Liu

Journal of Nuclear Materials, 577(2023), 154303.

Paper III: Microstructure and texture evolutions in FeCrAl cladding tube during pilger processing.

X. Qin, R. Zhang, P. Du, J. Pei, Q. Pan, Y. Cao, H. Liu

Journal of Materials Research and Technology, 25(2023), 5506-5519.

Contribution to the appended papers

Paper I – III: The author independently designed the experimental plan and conducted the experimental work. The author and co-authors performed the analysis of the results. The manuscript was written by the author and revised by the co-authors.

List of acronyms and abbreviations

ASS: Austenitic stainless steel

LTC: Low-temperature carburizing

HE: Hydrogen embrittlement

HIC: Hydrogen induced cracking

CW: Cold working

SA: Solution annealing

BCC: Body-centered cubic

FCC: Face-centered cubic

γ_C: Carbon stabilized expanded austenite (S-phase)

XRD: X-ray diffraction

EPMA: Electron probe micro-analyzer

XPS: X-ray photoelectron spectroscopy

SEM: Scanning electron microscope

EBSD: Electron backscattered diffraction

IPF: Inverse pole figure

IQ: Image quality

KAM: Kernel average misorientation

SSRT: Slow strain rate tensile

$R_{p0.2}$: 0.2% proof stress (0.2% offset yield strength)

R_m: Maximum tensile stress

δ: Total elongation

φ: Reduction of area

OCP: Open circle potential

E_{corr}: Corrosion potential

E_b: Breakdown potential

I_{corr}: Corrosion current density

Table of Contents

1 Introduction

1.1 Background

Austenitic stainless steels (ASS) are named for their face-centered cubic (FCC) crystal structure and excellent corrosion resistance [1]. In general, this type of steel contains high levels of chromium, nickel and other alloying elements which grant it excellent corrosion resistance, high ductility, good toughness, and formability [2]. It is used in a wide range of applications, including in chemical, food processing, nuclear and pharmaceutical industries. Due to low hydrogen diffusivity and excellent resistance to hydrogen embrittlement (HE) [3-5], ASS have also been widely used in high-pressure hydrogen applications. The susceptibility to HE strongly depends on the stability of the austenitic phase. Metastable ASS is susceptible to strain-induced martensitic transformation, resulting in increased susceptibility to corrosion and HE [6,7]. Type 316 stainless steels have better resistance to HE compared to metastable 304 owing to increased Ni and Cr concentrations, which suppress the strain-induced martensite transformation. However, from the cost point of view, AISI 304 is attractive because of the lower content of alloying elements.

Corrosion and HE are problems faced by steels in hydrogen applications. The hydrogen uptake in steels leads to the increase of surface activity and decomposition of the passive film, causing pitting corrosion and dissolution of stainless steels [8-10]. Hydrogen in the steel may also lower the stress required for cracks in the metal to initiate and propagate, resulting in premature failure. Hydrogen-assisted cracking is often imperceptible, which leads to severe catastrophic consequences. Understanding the corrosion behavior and hydrogen embrittlement of ASS and adopting effective approaches to mitigate it are crucial to the long service life.

In general, strategies to improve corrosion resistance and reduce hydrogen embrittlement mainly focus on composition design, processing technology and surface engineering [11-19]. Surface engineering may greatly improve the application potential of components. Bhadeshia [12] introduces an oxide layer with a thickness of 1-3 μm by performing black oxidation treatment on the steel surface. This oxide layer increases the atmospheric corrosion resistance of the steel and reduces hydrogen diffusion into the steel. The diffusion coefficient of hydrogen in coatings such as TiC [13], Al_2O_3 [14] and TiN [15] is 3-5 orders of magnitude lower than that in steels, which can improve the resistance to hydrogen embrittlement. However, the bonding strength between the coating and the substrate is the key to affecting hydrogen embrittlement susceptibility [16]. Surfaces mechanical or chemical heat treatment [17-20] is also a promising method to improve resistance to hydrogen embrittlement. For instance, shot peening introduces compressive stress on the steel surface, increasing the density of hydrogen trap sites. Due to the blocking effect of the shot peening layer, the intrusion of hydrogen into the matrix in the steel is limited, and the alloy shows lower HE sensitivity [17] [18]. Another surface modification technique, surface nitriding, can stabilize the austenite phase and prevent the transformation of unstable 301 and 304 stainless steel from austenite to martensite [19]. In addition, interstitial nitrogen atoms reduce the lattice spacing, creating compressive stress on the surface. Consequently, the treated alloy exhibits high resistance to HE.

Low-temperature carburizing (LTC), as a surface chemical heat treatment technology, is simple to operate and low in cost. It has been proven to improve the corrosion and mechanical properties [20] of the steels. By introducing expanded austenite into ASS through LTC, a supersaturated solid solution with high concentration of interstitial carbon, also known as S-phase can be obtained. This phase

exhibits improved mechanical properties such as hardness, wear and fatigue resistance while retaining corrosion resistance [21]. Therefore, it is of great interest to examine the effect of LTC on corrosion and hydrogen embrittlement resistance of ASS. The current research on expanded austenite mainly focuses on microstructure characterization and surface properties such as fatigue and tribological properties. The corrosion and mechanical behaviors of metastable AISI304 austenitic stainless steels after LTC in hydrogen environment are rarely reported, although low-cost AISI 304 has been widely used commercially. This study will discuss in detail the corrosion and hydrogen embrittlement of LTC samples after hydrogen uptake.

1.2 Objectives

The research objective is to evaluate the feasibility of LTC on alleviation of hydrogen embrittlement and corrosion for commercial austenitic stainless steel 304. In this study, mechanical properties, corrosion behavior, and microstructure of the S phase in AISI 304 after hydrogen uptake have been studied and linked. The following work has been performed:

- Characterization of S-phase on selected Austenitic stainless steel – AISI 304.
- Evaluation of the resistance to hydrogen embrittlement of S-phase, and comparison with the steel without LTC treatment.
- Evaluation of the effect of hydrogen uptake on corrosion behavior of S-phase, and comparison with the steel without LTC treatment.

2 Materials and processes

2.1 Stainless steel

2.1.1 General aspects

Stainless steel is a chromium-containing iron-based alloy known for its high resistance to corrosion and rust. The dense chromium oxide that forms on the surface of stainless steel makes it ideal for use in harsh environments or when exposed to moisture. Stainless steel [22] was first developed by British metallurgist Harry Brearley. He discovered that adding chromium to iron and carbon could produce corrosion-resistant steel. He named this new material "stainless steel". Stainless steel was developed to solve a major problem in many industries where tools and equipment rust and corrode. Today, stainless steel is one of the most widely used materials in the world, from medical equipment and surgical tools to automotive parts and aerospace components. Its durability, corrosion resistance and aesthetic appeal make it an attractive material for a variety of industries.

The performance of stainless steel is closely related to chemical composition and microstructure. In general, alloying elements in stainless steel include Cr, Ni, Mo, Ti, Si, N and C [23]. Cr is the most important alloying element in stainless steel, and the minimum amount of Cr required to form protective passive oxide film is ~11%. The more chromium that is added, the more corrosion-resistant the steel becomes. However, high Cr levels may accelerate the formation of Cr-rich α'/σ phase, leading to embrittlement of stainless steel. Ni is added to improve ductility, toughness, and resistance to corrosion and high temperatures. Mo is added to improve resistance to pitting and crevice corrosion in chloride environments. It also improves the high-temperature strength of the steel. Addition of Ti can improve corrosion resistance and stabilize the austenitic phase of the steel. N is added to improve corrosion resistance and to increase the strength of the steel. C can improve the hardness and strength of the steel. However, too much carbon can decrease the corrosion resistance of the steel. These alloying elements are classified as ferrite stabilizers and austenite stabilizers based on their effect on the microstructure. Ferrite-stabilizing elements include Cr, Mo, Si and Ti, among others. Austenite stabilizing elements include Ni, Mn, C and N. The Schaeffler-Delong diagram [24] (Figure 2.1) gives the phase stability of austenite and ferrite based on "Ni-equivalent" and "Cr-equivalent" (see equations in the figure). It is an empirical diagram that can intuitively reflect the influence of various alloying elements on the microstructure of stainless steels. Type 304 is a metastable austenitic stainless steel located in the austenite and ferrite regions, while type 316 is austenitic stainless steel located in the austenite as shown in Figure 2.1. Note that this empirical rule is based on equilibrium conditions and does not consider the effects of non-equilibrium factors such as deformation and quick cooling. In general, increasing the content of ferrite in stainless steel can improve its strength and magnetism, while increasing the content of austenite can improve its ductility, formability, and corrosion resistance.

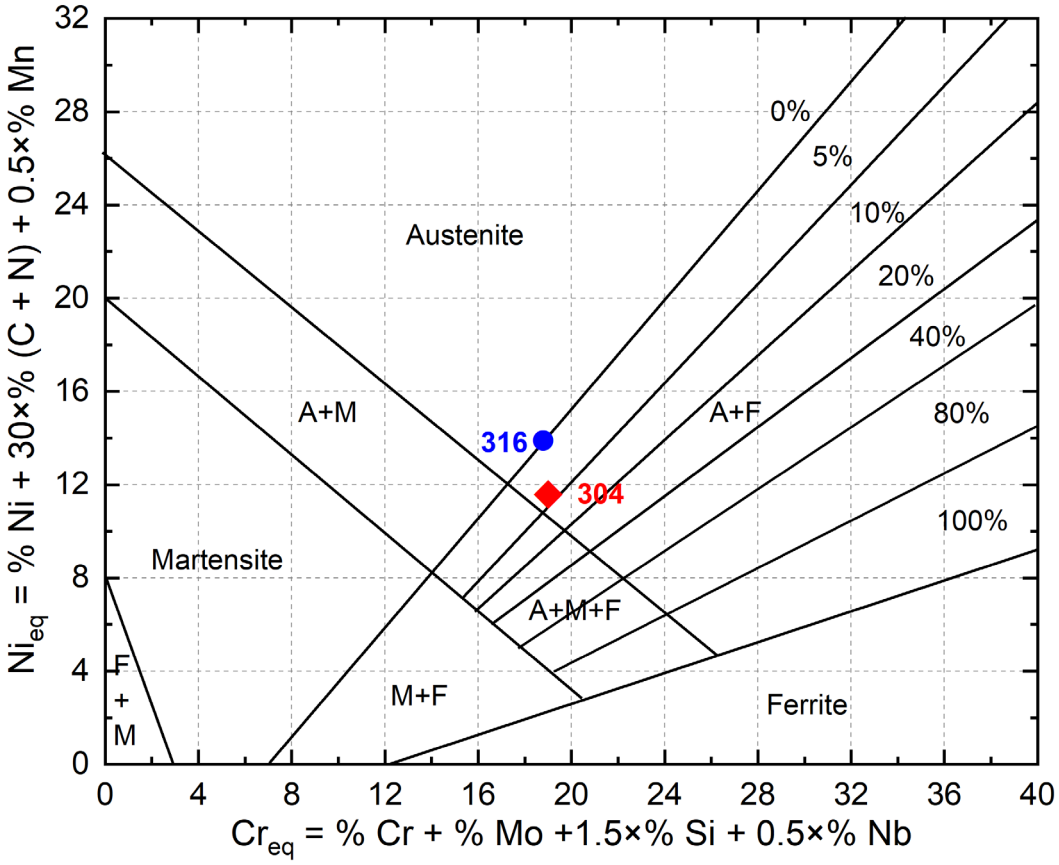

Figure 2.1 Schaeffler-Delong diagram redrawn from reference [24]. 304 and 316 are marked.

2.1.2 Classification of stainless steels

Stainless steels are classified into different grades based on their chemical composition, physical properties, and intended application. Based on the microstructure stainless steel can be divided into five grades: austenitic, ferritic, martensitic, duplex and precipitation hardening [25]. Each type of stainless steel has its unique properties and characteristics.

Austenitic Stainless Steel: It contains sufficient amount of nickel and / or manganese and nitrogen to achieve a face-centered cubic crystal structure. This steel maintains an austenitic microstructure at all temperatures from room temperature to melting temperature. Therefore, austenitic stainless steels cannot be hardened by heat treatment because they have single FCC phase at all temperatures. Austenitic stainless steels are the largest family of stainless steels, accounting for approximately two-thirds of all stainless steel production. Referring to ASTM standards, austenitic stainless steels are divided into 200 series and 300 series:

a) The 200 series are Cr-Mn-Ni alloy that maximizes the use of Mn and N and minimizes the use of Ni. Their yield strength is approximately 50% higher than that of the 300 series due to the addition of nitrogen.
b) The 300 series are Cr-Ni alloys that achieve their austenitic microstructure almost entirely by nickel addition. Some very highly alloyed grades include nitrogen to reduce the demand of nickel. The 300 series is the largest group and the most widely used.

Ferritic Stainless Steel: This type of stainless steel contains high levels of Cr (10.5~27 wt.%) with very little or no Ni. Ferritic stainless steels have a body-centered cubic (BCC) structure and mainly belong to

the 400 series. Niobium (Nb), titanium (Ti) and zirconium (Zr) are added to prevent the formation of Cr-rich carbides and improve weldability. Compared with austenitic stainless steels, they have relatively poor corrosion resistance and plasticity due to their low alloying elements and bcc structure. They are often used in automotive exhaust pipes, heat exchangers and building structural applications [26].

Martensitic Stainless Steel: Martensitic stainless steel has a body-centered tetragonal (BCT) crystal structure and is ferro magnetic as ferritic steel. Due to their low chromium content, they are not as corrosion resistant as ferritic and austenitic stainless steels. Martensitic stainless steels have high strength and hardness and are used as tool steels and creep-resistant steels. The Fe-Cr-C and Fe-Cr-Ni-C alloys are the main series of martensitic stainless steels. Some of the carbon is replaced by nickel for greater toughness and higher corrosion resistance. Minor additions of Nb, V, B and Co increase strength and creep resistance up to about 650 °C. Martensitic stainless steels can be heat treated to provide better mechanical properties. Heat treatment usually consists of three steps: austenitizing, quenching and tempering. The steel is heated to temperatures in the range of 980~1050 °C and the C redissolves into the face-centered cubic lattice to form austenite. After quenching, the austenite transforms into martensite. Quenched martensite is very hard but too brittle. Therefore, martensite is heated to around 500 °C, held at that temperature, and air-cooled to obtain tempered martensite to improve the ductility and toughness. Higher tempering temperatures reduce yield strength and ultimate tensile strength but increase elongation and impact toughness.

Duplex Stainless Steel: Duplex stainless steels have a mixed microstructure of austenite and ferrite. The ratio of the two phases depends on the nickel and chromium equivalents. Compared to austenitic stainless steels, they have higher levels of Cr (19–32%) and Mo (up to 5%) but are lower in Ni content. The mixed microstructure of duplex stainless steels improves yield strength and resistance to stress corrosion cracking in a Cl^- environment. This kind of steel is often used in chemical processing equipment and the oil and gas industry [27].

Precipitation Hardening Stainless Steel: Precipitation-hardening stainless steels can achieve higher strength than martensitic grades by precipitation hardening. There are three types:

a) Martensitic 17-4 PH (17Cr-4Ni-4Cu-0.3Nb, wt%) used in aerospace. The Nb- and Cu-rich precipitates are formed by aging, which increases the yield strength above 1000 MPa.
b) Semi-austenitic 17-7 PH (17Cr-7.2Ni-1.2Al, wt%). The Ni_3Al intermetallic phase is precipitated, reaching a yield strength above 1400 MPa.
c) Austenitic A286 (15Cr-25Ni-2.1Ti-1.2Mo-1.3V, wt%). Ni_3Ti precipitates improve mechanical properties and creep resistance at temperatures up to 700 °C. A286 is classified as an iron-based superalloy used in jet engines, gas turbines, and turbine components.

2.2 Commonly used austenitic stainless steel grades

The most commonly used austenitic stainless steels are AISI 304 and 316.

2.2.1 AISI 304

Type 304, also known as AISI/SAEs 304, UNS S30400 and EN 1.4301, is the most widely used stainless steel in the market. It contains both Cr (18~20%) and Ni (8~10.5%) and is also known as 18/8 steel. AISI 304 is commonly used for applications such as kitchen, food processing, chemical containers, and medical equipment due to its excellent corrosion resistance, high ductility, and good mechanical properties.

AISI304 is a metastable austenitic stainless steel and is prone to deformation-induced martensite. For the 304 ASS used in this study, in addition to the dominant austenite phase, the XRD and EBSD results in Figure 2.2 confirms that it contains a small amount of ferrite, which is consistent with the prediction in Figure 2.1.

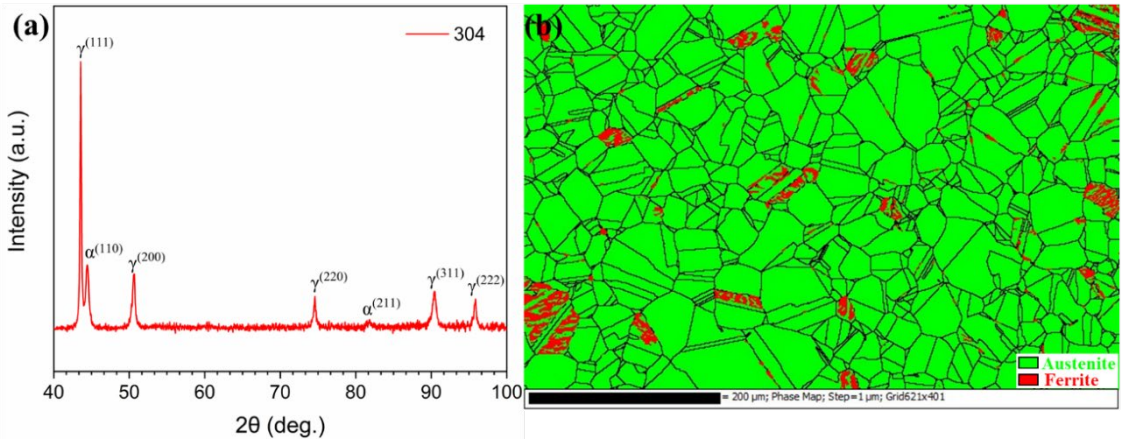

Figure 2.2 XRD (a) and EBSD-phase map (b) of solution annealed 304 austenitic stainless steel.

2.2.2 AISI 316

Type 316 also known as AISI/SAE 316 UNS S31603 and EN 1.4404, is an evolution of type 304. It contains Cr (16~18%), Ni (10~14%), Mo (2~3%), and small quantities of carbon (≤0.03%). AISI 316 has better corrosion resistance than AISI 304, especially in chloride-rich environments. AISI 316 is typically used in applications requiring enhanced corrosion resistance such as marine equipment, chemical processing, pharmaceuticals, medical equipment, and certain types of food processing equipment.

A typical 316 microstructure is shown in Figure 2.3. The IPF map (Figure 2.3a) shows equiaxed grains with various orientations, indicating that the microstructure is homogeneous. A large number of twin structures are observed within the grains. Due to its higher nickel equivalent than 304, it shows a stable austenite phase (Figure 2.3b).

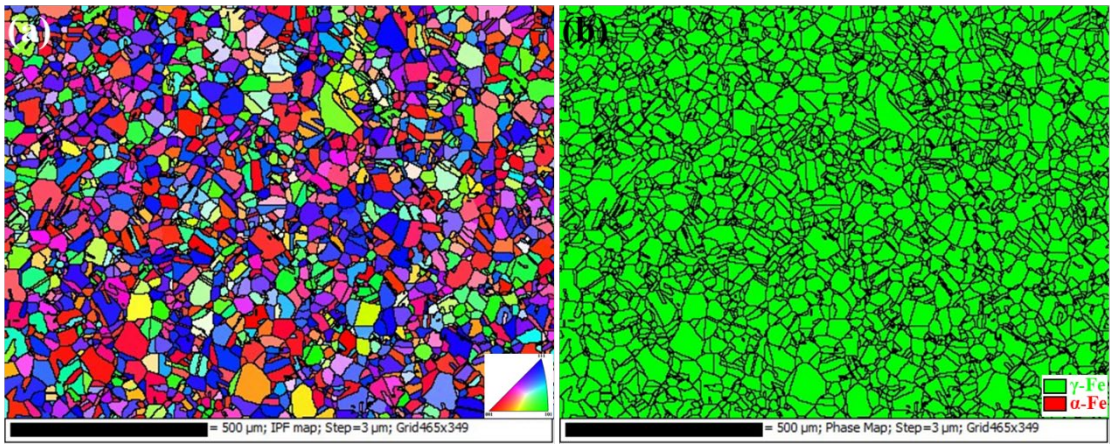

Figure 2.3 IPF map (a) and phase map (b) of solution annealed 316 austenitic stainless steel.

2.3 Low-temperature carburizing

2.3.1 Overview

Low-temperature carburising (LTC) is a surface hardening process through the diffusion of interstitial carbon, without the possible formation of carbides. This process results in a hard carburised layer with a thickness of 20 ~ 35 μm on the surface [20,21]. The carbon content on the surface of the carburised layer exceeds 20 at.% due to the existence of supersaturated interstitial carbon. The LTC process involves activation of the surface followed by a gas-phase carburization treatment. Surface activation is to remove the chromium oxide layer so that carbon can diffuse into the substrate, because the chromium oxide layer on the surface of stainless steel is the main obstacle to LTC. In industrial processes, activation can be achieved by exposing the furnace load to a halide-containing gas mixture (NF_3 or HCl and N_2) at atmospheric pressure. Conventionally, carburization is otherwise performed at relatively high temperatures to maximize solubility and diffusion rates of interstitial carbon solute.

Figure 2.4 shows the time-temperature transformation (TTT) diagram for the heat treatment of austenitic stainless steels [28]. In general, the maximum equilibrium solubility of C in austenitic stainless steels is 0.08 wt% (0.37 at%), which is limited by the formation of chromium carbides ($Cr_{23}C_6$) or χ/ω-carbides in the steel matrix. These carbides can lead to a loss of corrosion resistance and mechanical properties. For carburising at high temperatures (T > 1650 °F, or 900 °C), carbide precipitation can only be avoided by extremely high cooling rates (path A). In addition, the solubility limit is easily exceeded at high temperatures and carbides are formed during carburization. However, at industrial cooling rates most of the solute atoms will precipitate into the carbide (path B), which depletes chromium and reduces corrosion resistance in austenitic stainless steels. LTC, on the other hand, obtains a carburised layer while suppressing the formation of chromium-rich carbides (path C). This results in extremely high carbon supersaturation, much higher than can be achieved by high temperature carburising. At 350 to 500 °C, the diffusivity of Ni and Cr is on the order of 10^{-21} m^2/s and 10^{-22} m^2/s, respectively, and the carbon diffusivity at this temperature is in the range between 10^{-10} to 10^{-12} m^2/s [29-31]. This difference in diffusion coefficient by a factor of 10^{10} to 10^{12} enables uniform carburization of austenitic stainless steels without forming carbides.

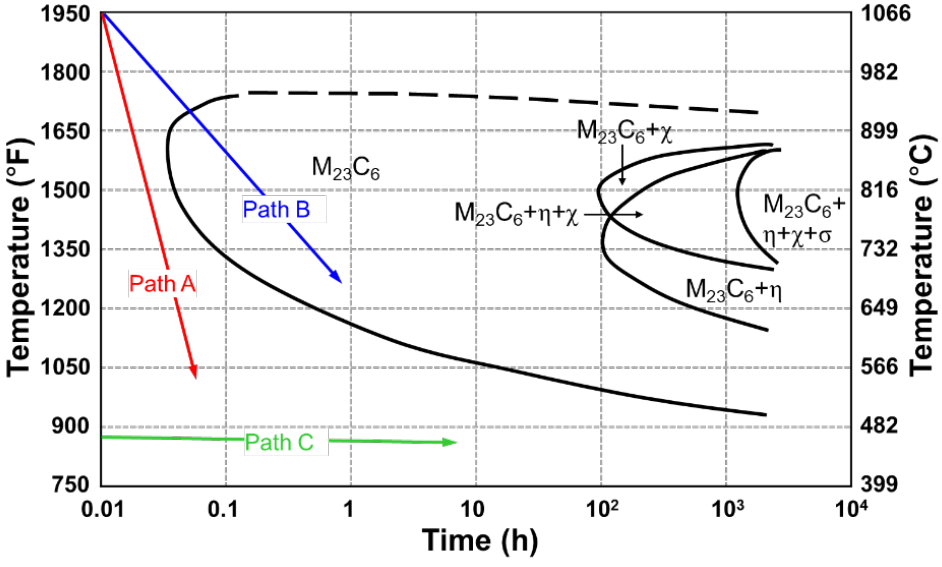

Figure 2.4 Time-temperature-transformation (TTT) diagram of carbide formation in austenitic stainless steels (Redrawn from [28]).

In this work, the low temperature carburizing process was performed with Bodycote's Kolsterising® S^3P K22 treatment [32]. The key process parameters are confidential. It is claimed that when forming C supersaturated austenite without Cr-rich precipitates, surface harnesses can reach up to 1200 HV with diffusion layer thicknesses between 20 µm and 30 µm.

2.3.2 Carbon stabilized expanded austenite

Carbon-stabilized expanded austenite (γ_c), also known as S-phase, is a supersaturated carbon solution in austenite. The S-phase with high carbon concentration (~20 at.%) and super-hardness (≥ 900 HV) on the surface is used to improve the wear resistance and fatigue strength of steel components [21]. Supersaturated carbon changes the austenite lattice parameters, as indicated by the peak shift in XRD pattern (Fig, 2.5) The linear dependence between the austenite lattice parameter (a) and the interstitial C content can be expressed by equation 2.1 [33]:

$$a = 0.35965 + 0.06029y_c \qquad (2.1)$$

where y_c is the octahedral interstitial occupancy of C. Note that this condition is based on highly controlled carburizing which ensures uniform interstitial carbon content throughout the steels and therefore eliminates concentration and stress gradients. Thin metal foil (< 100 µm) is used as the substrate in this case. Otherwise, the bulk-limited lattice expansion prevents homogeneous carburization throughout the materials. The interstitial concentration gradient induced by the diffusion process leads to a compressive residual stress gradient through the expanded austenite layer. Beneath the interstitial enriched region, tensile residual stress will exist. As a balance, very high residual compressive stresses (> 2 GPa) occur in subsurface regions [34]. The increase in lattice parameters and strain causes the X-ray diffraction peaks to shift to lower angles and broadens the peak compared to the untreated sample.

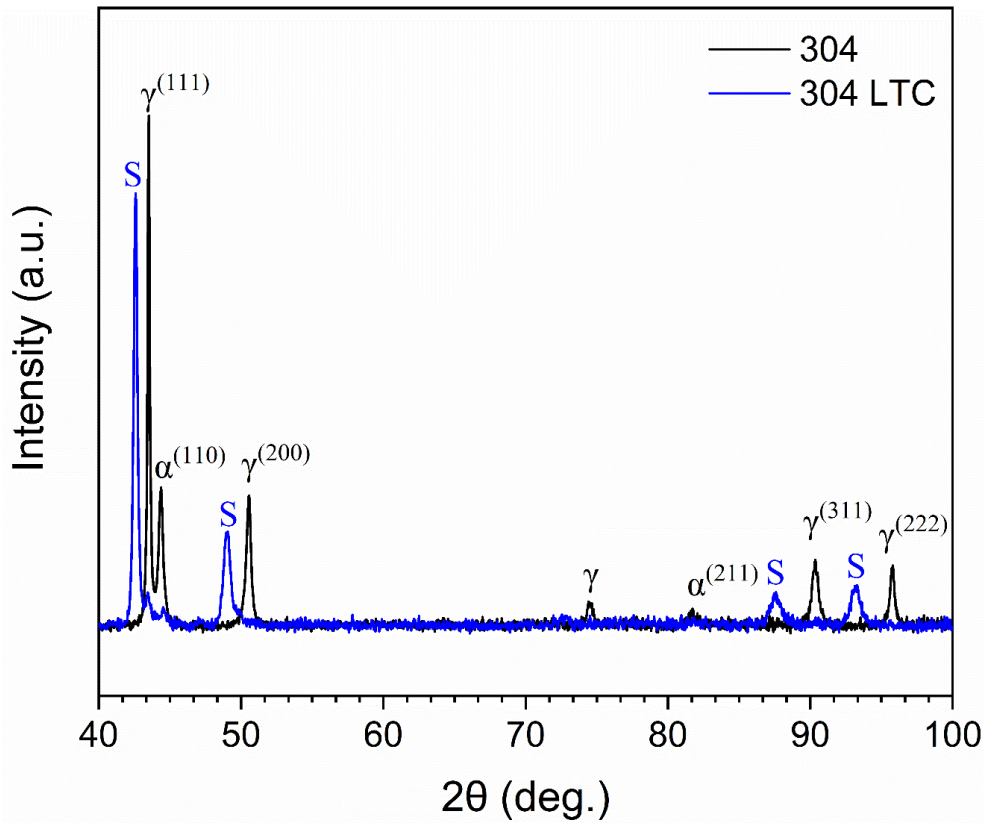

Figure 2.5 XRD patterns from solution annealed 304 with and without LTC treatment.

The microstructure of solution annealed 304 LTC is given in Figure 2.6, showing that the thickness of expanded austenite (γ_c) is ~22 μm. Gradient orientations and high local misorientation were presented in γ_c.

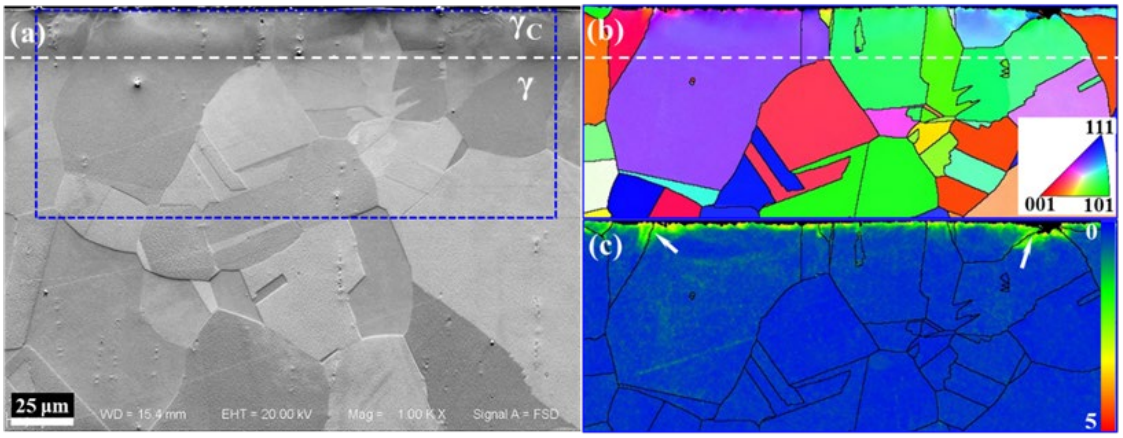

Figure 2.6 Cross-section microstructure of solution annealed 304 LTC. (a) FSD image, (b) IPF map and (c) KAM map.

2.3.3 Properties of S-phase

The S-phase has a thickness of ~ 25 μm near the surface of the processed component. In the literature, the properties related to the S-phase mainly focus on mechanical, tribological and corrosion properties.

Mechanical properties

The remarkable mechanical property of the S-phase is the extremely high surface hardness. Numerous studies [20,21,35-37] have reported that the hardness of the S-phase can reach up to about 1000 HV. This is attributed to work hardening due to local deformation introduced by interstitial carbon and residual stress. The hardness gradually decreases with the depth from the surface, as depicted in Figure 2.7a, indicating that the S-phase is a diffusion-controlled gradient layer.

Tensile characteristics are important mechanical properties of concern for structural materials. The formation of S-phase may enhance the tensile strength; however, it results in a loss of ductility as shown in Figure 2.7b. Strength and plasticity have always been difficult to achieve at the same time. Defects introduced by the S-phase such as high dislocation density and lattice distortion make the slip of dislocations more difficult, greatly improving the strength. On the other hand, the large lattice mismatch between the S-phase and the matrix makes it hard to coordinate deformation, resulting in a decrease in ductility.

Excellent fatigue resistance is also an important advantage of the S-phase. High surface residual compressive stress up to 2 GPa can be introduced through LTC [37]. It has been reported that the high cycle fatigue life of the LTC treated 316 is approximately 100 times that of untreated 316. In addition, maximum fatigue stress increased by ~75% from 200 MPa to 350 MPa [38]. The crack growth threshold ΔK_{th} was increased from 8 MPa·m$^{1/2}$ to 10 MPa·m$^{1/2}$ by LTC for 316 [39].

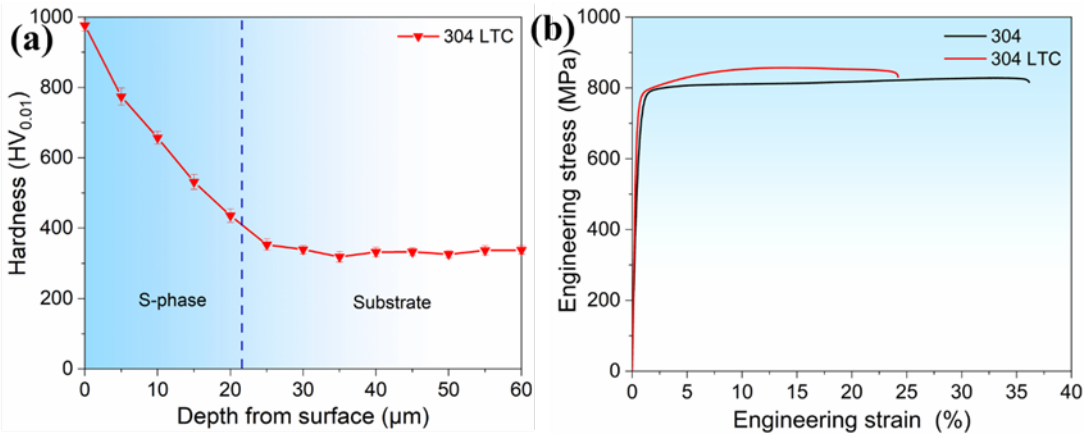

Figure 2.7 Microhardness profiles (a) and stress-strain curve (b) from cold worked 304 with LTC treatment.

Tribological properties

The poor tribological properties of austenitic stainless steels limit their applications. The S-phase exhibits high hardness, resulting in improved tribological properties. Sliding friction and reciprocating friction tests show that the wear rate of the coupled 316L parts (ball and disc) treated by LTC is reduced by approximately 100 times compared to untreated 316L [40,41]. In addition, the untreated material suffered severe plastic deformation and large pieces of wear debris peeled off during the test, while the carburized material did not.

Corrosion resistance

S-phase has excellent corrosion resistance. Often, a featureless layer is found from the metallographic microstructure after chemical etching. It has been reported that pitting potential is increased in chloride-containing solutions compared to the austenitic stainless-steel matrix [40-43]. This can be explained by the high carbon concentration on the surface. Carbon may form partial (covalent) bonds with metal atoms (Fe, Cr, Ni), inhibiting the dissolution of iron [44]. Crevice corrosion is a potential failure mode of austenitic stainless steel. It has been shown that the S-phase improves the crevice corrosion resistance as well [45].

The potentiodynamic polarization curve shown in Figure 2.8a indicates that LTC treatment increases corrosion potential and pitting corrosion potential for 304. Figure 2.8b shows that the 304 has large corrosion pits while the 304 with LTC treatment has almost no serious pitting corrosion, confirming again that S-phase has excellent corrosion resistance.

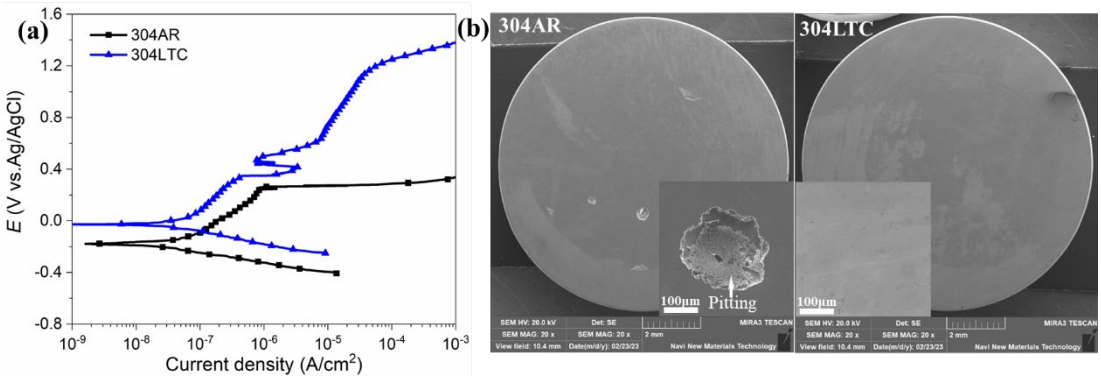

Figure 2.8 (a) Potentiodynamic polarization curves of 304 samples in 3.5% NaCl solution, and (b) SEM images after corrosion.

3 Challenges of hydrogen uptake

Hydrogen uptake can occur when steel is exposed to hydrogen-containing environments. Hydrogen enters the steel mainly through the following processes [46]. The corresponding activation energy (ΔQ) is also provided for each step in Eq. 3.1 – 3.4

1. Hydrogen molecules (H_2) collide with the outer surface of the metal (M), causing physical adsorption (Eq.3.1).

$$H_2 + M \rightleftharpoons H_2 \cdot M \quad \Delta Q_1 = -(8 - 12)\ \text{kJ/mol} \tag{3.1}$$

2. Further chemical adsorption with the metal occurs. Covalently adsorbed hydrogen ($H_{ad}M$) is generated (Eq.3.2).

$$H_2M \rightleftharpoons H_{ad}M + H_{ad} \quad \Delta Q_2 = -(29 - 42)\ \text{kJ/mol} \tag{3.2}$$

3. Covalently adsorbed hydrogen is converted into dissolved absorbed hydrogen (MH_{ab}) (Eq.3.3).

$$H_{ad}M \rightleftharpoons MH_{ab} \quad \Delta Q_3 = -(10 - 20)\ \text{kJ/mol} \tag{3.3}$$

4. The hydrogen atoms decouple from the metal M in the surface and become dissolved hydrogen (H) in the bulk metal phase (Eq.3.4).

$$MH_{ab} \rightleftharpoons M + H \quad \Delta Q_4 = -10\ \text{kJ/mol} \tag{3.4}$$

Hydrogen has high activity, and the small atomic radius means it can easily penetrate steel. Hydrogen can be trapped at various types of lattice defects such as vacancies and certain solutes, dislocations, grain boundaries, phase interfaces, triple points, precipitates, micro- and nanocracks, surface steps, voids and the inside surface oxide layers (Figure 3.1). Hydrogen uptake in materials such as metals and alloys, can pose several challenges, including hydrogen embrittlement and corrosion.

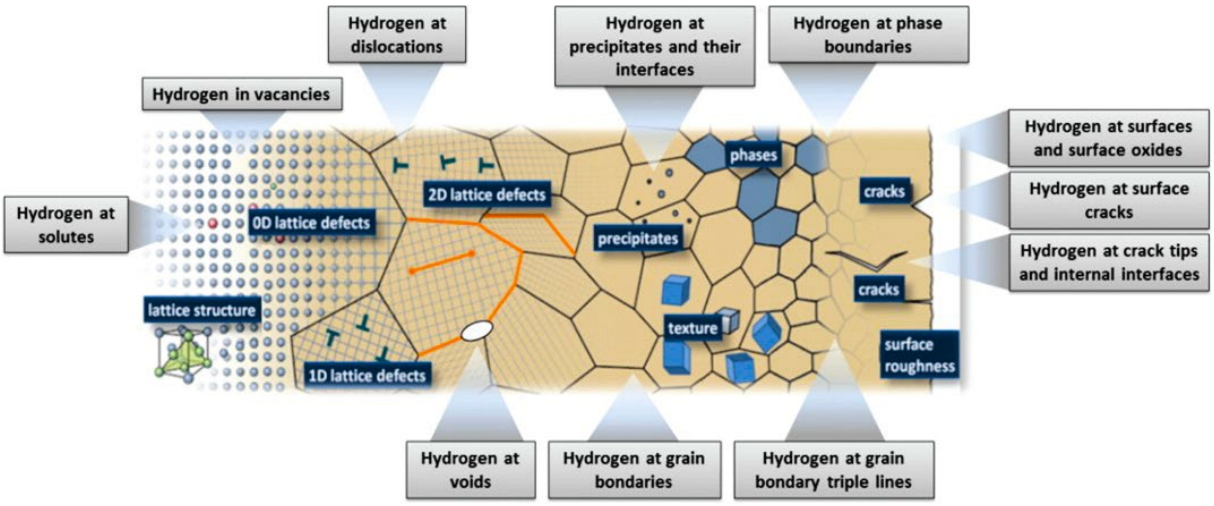

Figure 3.1 The distribution of hydrogen within the bulk material. Reproduced from reference [47], with the permission of Taylor & Francis

3.1 General corrosion and the effect of hydrogen

Corrosion is a gradual deterioration of materials (mostly metallic materials) through chemical or electrochemical reactions with their environment [48]. It causes damage to metal surfaces and reduces the service life of structural components. The total global cost of corrosion is estimated to be

approximately $ 2.5 trillion, which is equivalent to 3.4% of the global GDP (2013). Economic losses and environmental damage caused by corrosion threaten human health and development [49]. Therefore, it is of great significance to study the corrosion behavior and improve the corrosion resistance of metallic materials.

Michael Faraday established the principles of the electrochemical process of corrosion in the early 19th century, and it remains critical to understanding the problem and preventing corrosion [50]. The corrosion process [51] consists of anodic and cathodic half-cell reactions. In anodic reaction metal (M) corrodes and enters the solution (electrolyte) in the form of positively charged metal ions (M^{n+}), as shown in Eq.3.5.

$$\mathrm{M} \rightarrow \mathrm{M}^{n+} + ne^{-} \tag{3.5}$$

The cathodic reaction depends on the chemical nature of corrosives and most commonly occurs in nature and in neutral or alkaline solutions, namely the reduction of dissolved oxygen, as shown in Eq.3.6.

$$\mathrm{O}_2 + 2H_2O + 4e^{-} \rightarrow 4\mathrm{OH}^{-} \tag{3.6}$$

In acids, the cathode reaction is the reduction of hydrogen ions, as given in Eq.3.7.

$$2\mathrm{H}^{+} + 2e^{-} \rightarrow \mathrm{H}_2 \uparrow \tag{3.7}$$

In electrochemical tests, an oxidation process occurs when a metal acting as the anode in a corrosion cell becomes polarized, causing its electrode potential to shift toward the inert (cathode) direction. Likewise, if a metal is made a cathode by applying a negative current across it, its electrical potential decreases, i.e., cathodic protection.

Potentiodynamic polarization curves are often used to evaluate corrosion behavior. Electrochemical parameters such as corrosion current and corrosion potential can be obtained from the Tafel curve. Tafel has shown that polarization obeys the Eq.3.8 [52].

$$\eta = \pm A \log_{10}\left(\frac{i}{i_0}\right) \tag{3.8}$$

where η is the overpotential, A is Tafel slope, i is the current density, and i_0 is the exchange current density. The +/- sign depicted in the equation relates to whether the analysis refers to an anodic (+) or cathodic (-) process.

Figure 3.2 illustrates graphically some parameters which are often used in discussion of electrochemical corrosion. In the Tafel curve (Figure 3.2a), there are two half-reactions. In an acidic solution, a hydrogen evolution reaction occurs at the cathode, and metal dissolution occurs at the anode. The corrosion potential E_{corr} is usually equal to the open circuit potential, and the corrosion current density i_{corr} is the one corresponding to the intercept between the Tafel slope and the corrosion potential. Figure 3.2b reveals the entire corrosion process of metal. For self-passivating alloys (such as stainless steel), a film of corrosion products forms on their surfaces, greatly protecting them from further attack. In a passivation process, the metal first corrodes at an extremely high rate with increased anodic current density until it reaches a critical value i_{CC} , corresponding to the formation of a passivation film in a thickness of a few nm on the entire surface. The corresponding potential at this point is primary passivation potential (E_{PP}). After that, the metal no longer obeys Tafel's equation. As the potential increases, the corrosion current density drops sharply to passive current density (i_P). Once the applied potential exceeds the passivation potential or the passivation film is damaged, the metal may begin to corrode rapidly again [54].

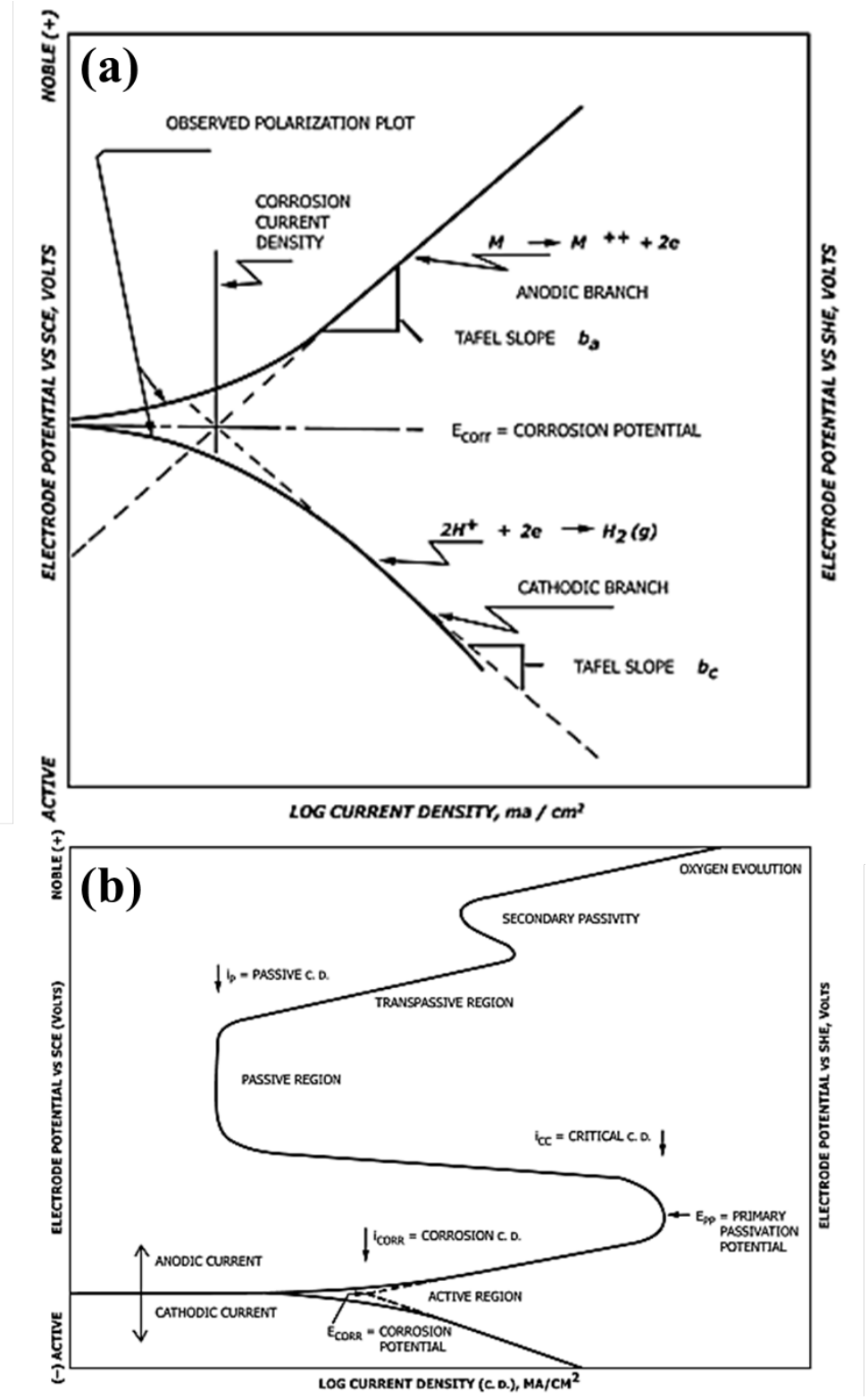

Figure 3.2 Polarization diagram. (a) Tafel curve and (b) Potentiodynamic polarization curve. Reproduced from ASTM G3-14 [53].

For steels exposed to a hydrogen environment, a series of performance degradation may occur. The obvious effect of hydrogen on the corrosion behavior of iron and stainless steel is that hydrogen increases the corrosion rate, reduces the stability of the passive film, and promotes localized corrosion [55,56]. Thomas et al. [57] found that hydrogen uptake resulted in an increased anodic dissolution of

AISI 1018 mild steel in a flowing non-passivating electrolyte (0.6 M NaCl, pH 1.95) by approximately 200 - 500%. He et al. [58] studied the crevice corrosion behavior of duplex stainless steel 2205 after hydrogen charging, and the results showed that hydrogen can promote the initiation and propagation of crevice corrosion and inhibit the re-passivation process. This can be explained by the multiple effects of hydrogen permeation on the stability of the passivation film, such as reduced thickness, increased carrier density, and lowered the ratio of Cr cation and O/OH ratio of the passivation film.

3.2 Hydrogen embrittlement

3.2.1 Stage of hydrogen embrittlement

The phenomenon of hydrogen embrittlement was first observed and documented in the late 19th century [59]. It was noticed that certain alloys and high-strength steels became brittle and failed prematurely when exposed to hydrogen gas. Hydrogen embrittlement (HE), also known as hydrogen-induced cracking (HIC), occurs when a metal absorbs hydrogen and reduces the stress required for crack initiation and propagation, resulting in embrittlement. Hydrogen embrittlement occurs most notably in steel as well as iron, nickel, titanium, cobalt and their alloys. There are a series of stages involved in hydrogen embrittlement in a material as given below,

Hydrogen absorption

Hydrogen absorption is the first stage of hydrogen embrittlement. There are two main sources of hydrogen: internal hydrogen and external hydrogen. The former one is introduced during material manufacturing or surface treatment, such as electroplating, pickling and reduction heat treatment. The latter is hydrogen from sources such as the environment or cathodic protection systems during application.

Hydrogen diffusion

Once hydrogen is absorbed by a material, it can diffuse into the lattice structure. The rate of hydrogen diffusion depends on factors such as defects, crystal structure, temperature, and material composition etc.

Hydrogen capture

Hydrogen atoms can become trapped in various locations within the material, including vacancies and certain solutes, dislocations, grain boundaries, phase interfaces, triple points, precipitates, micro- and nano-cracks, and voids. Some of these defects, such as precipitated phases, act as hydrogen traps to inhibit hydrogen embrittlement, while others, such as micropores, interact with hydrogen and initiate cracks.

Crack initiation

Elevated stress concentrations caused by trapped hydrogen atoms may promote the creation of small cracks or fissures within the material. These cracks likely initiate at the place where the hydrogen is trapped.

Crack propagation

Under an applied load or stress, hydrogen-induced cracks can propagate in the material. These cracks can grow rapidly, even at stress levels significantly lower than the ones that cause failure in hydrogen-free material.

Reduced ductility

In the presence of hydrogen, the material becomes more brittle and less able to absorb energy through plastic deformation. Therefore, the ductility of the material decreases.

3.2.2 Hydrogen embrittlement mechanisms

Hydrogen-enhanced decohesion (HEDE)

In 1926, Pfeil [60] stated that absorbed hydrogen weakens grain boundaries and decreases cohesion across the cubic cleavage plane, leading to hydrogen-induced cracking. In 1959, Troiano [61] proposed that hydrogen weakens the interatomic bonds of iron atoms because the electrons in the 1s orbital of hydrogen atoms enter the 3d orbital of iron (the electrons in the 3d orbital of iron are not filled fully). This mechanism was further quantitatively developed by Oriani, McMahon and Gerberich [62-64], who believe interstitial hydrogen reduces the stress required for the separation of atoms (decohesion). HEDE occurs only when the local concentration of hydrogen is high. Notice, hydrogen solubility can be increased in the tensile stress field at a crack tip, at stress concentrators, or in the tension field of edge dislocations. Figure 3.3 illustrates the HEDE mechanism. Atoms are separated owing to the weakening of interatomic bonds by (i) hydrogen in the crystal lattice (ii) adsorbed hydrogen and (iii) hydrogen at the particle-matrix interface.

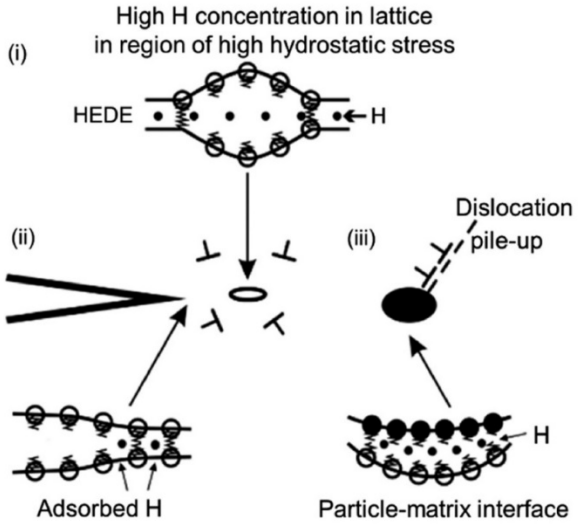

Figure 3.3 Schematic diagram of the HEDE mechanism. Tensile separation of atoms due to weakening of interatomic bonds by (i) hydrogen in the crystal lattice (ii) adsorbed hydrogen and (iii) hydrogen at the particle-matrix interface. Reproduced from [65] with permission from Elsevier.

Hydrogen-enhanced localized plasticity (HELP)

In 1972, based on the observation and analysis of fractures, Beachem [66] proposed that "hydrogen-assisted cracking of metals is caused by local plastic deformation facilitated by solute hydrogen at a crack tip". Later, Bimbaum, Robertson, and Sofronis [67-70] performed in-situ TEM in a gaseous

hydrogen environment and verified that hydrogen can reduce the stress required for dislocation movement or increase dislocation activity. High hydrostatic pressure at the crack tip results in hydrogen accumulation and consequently high hydrogen concentration there. Subcritical crack growth occurs through hydrogen-induced localised microvoid coalescence (MVC) processes [71,72], as shown in Figure 3.4. It can be observed that the hydrogen-affected plastic zone is much smaller than the hydrogen-free plastic zone. This means that hydrogen causes small plastic deformation before fracture. The HELP mechanism indicates that the hydrogen-induced cracking is due to local plastic deformation rather than the simple breaking of atomic bonds of HEDE.

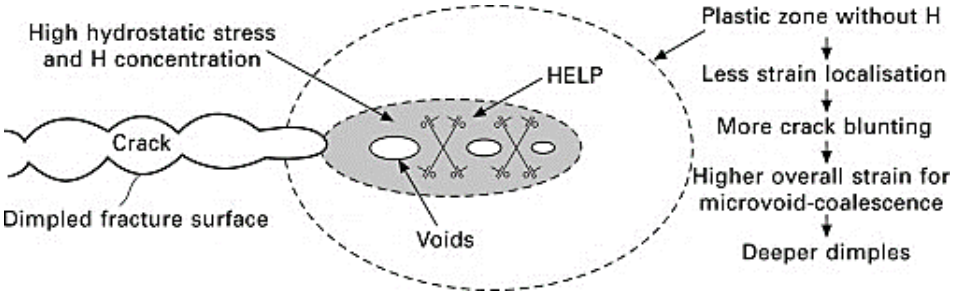

Figure 3.4 Schematic diagram illustrating the HELP mechanism. The region of high hydrogen concentrations facilitates the microviod coalescence process and localised plasticity. Reproduced from [72] with permission from Elsevier.

Adsorption-induced dislocation emission (AIDE)

The AIDE mechanism was first proposed by Lynch [73] in 1976 and was further developed in subsequent studies [74-76]. This mechanism is related to dislocation emission including dislocation generation and dislocation moving away from the crack tip. Dislocation is generated by the coordinated shear deformation of several atomic layers near the dislocation core. The adsorption of hydrogen leads to the weakening of the interatomic bonding, which accelerates dislocation emission and crack growth. The AIDE mechanism also involves the nucleation and growth of micro-voids at the crack tip. In a hydrogen-free environment, a large stress is required to initiate dislocation emission in the plastic zone near the crack tip. Conventional dislocation movement thus occurs, leading to the nucleation and growth of micro-voids at the interface of second phase and matrix, at the slip band, and in the plastic zone in front of the crack tip. In a hydrogen environment, hydrogen in the material weakens atomic bonds causing dislocations to easily emanate from the crack tip and promote crack development on appropriate slip planes. Therefore, lower stress is required to activate crack propagation. Moreover, hydrogen causes shallow dimples, intergranular or transgranular fractures. Figure 3.5 illustrates the schematic diagram of the AIDE mechanism at the crack tip [74].

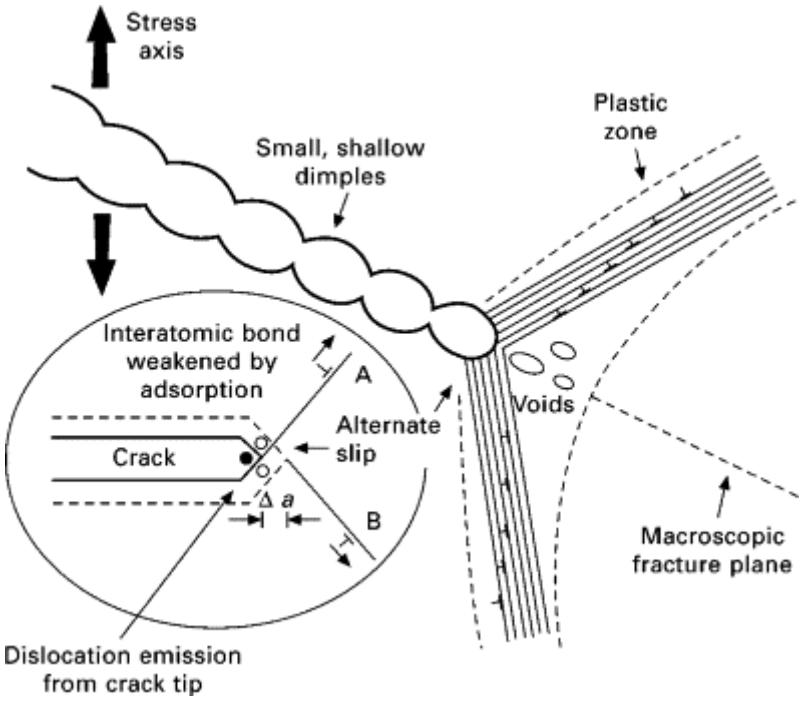

Figure 3.5 Schematic diagram illustrating the AIDE mechanism. The stress-induced crack grows by alternating slip (for transgranular paths) from crack tips, facilitating coalescence of the crack with the void formed in the plastic zone in front of the crack. Reproduced from [74] with permission from Elsevier.

Hydrogen-enhanced strain-induced vacancy (HESIV)

Nagumo [77,78] proposed that hydrogen enhances the generation of strain-induced vacancies, leading to crack initiation and growth. When combining with hydrogen, the mobility of vacancies is reduced thereby forming clusters that is in fact a void or reducing the stress-carrying capacity of the material. The HESIV mechanism shifts the view of HE from hydrogen itself to hydrogen-related damage which leads to premature fractures. A straightforward validation of the HESIV mechanism is experimental verification. It has been shown by low temperature thermal desorption spectroscopy (LTDS) in Figure 3.6a that the hydrogen content of hydrogen-charged martensitic steel without strain is 0.041 ppm. After pre-straining and then hydrogen charging, the hydrogen content of martensitic steel was 0.093 ppm. However, when hydrogen charging and straining were performed simultaneously, the hydrogen concentration was 0.20 ppm. A significant increased hydrogen content means increased vacancy concentration. Three-point bending tests on low-carbon ferritic steels with/without hydrogen show that the energy dissipation during crack growth (stable crack growth resistance curve) is significantly reduced due to hydrogen increased vacancy fraction (Figure 3.6b).

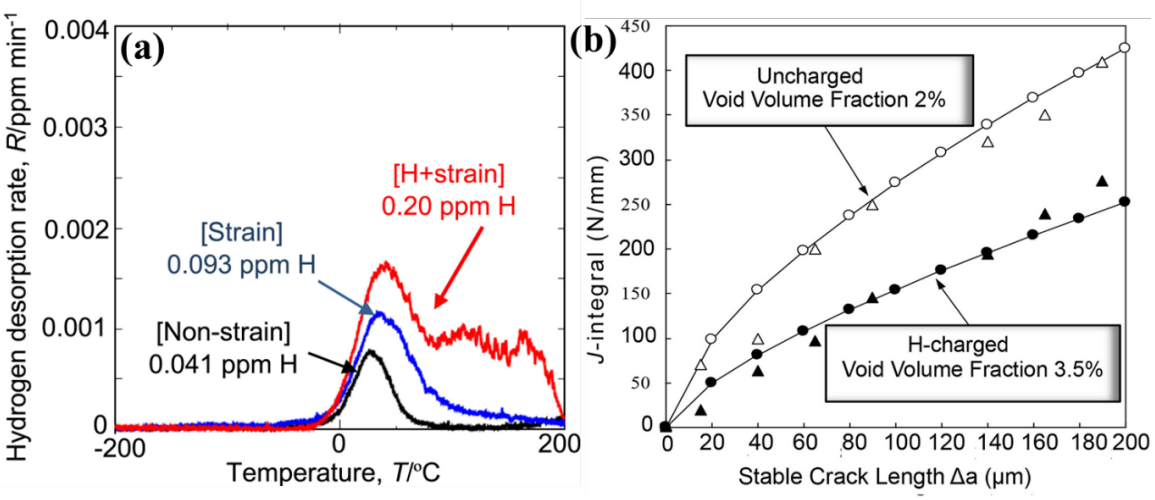

Figure 3.6 (a) LTDS curves of tracer-hydrogen for high strength martensitic steel [79]. (b) Experimental and calculated stable crack growth resistance of low carbon ferrite-pearlite steel with and without pre-charged hydrogen. ○, ●: Observed values, Δ, ▲: Calculated values using a finite element method [80]. Reproduced with permission from Elsevier.

Defect acting agent (DEFACTANT)

The DEFACTANT mechanism was proposed by Kirchheim based on the stabilization of lattice defects by hydrogen in a thermodynamic scheme [81-83]. Analogous to the Gibbs adsorption isotherm of surface energy changes caused by molecular adsorption, when solute atoms segregate at lattice defects, the total free energy of the system decreases. This reduction is attributed to the lowering of the defect formation energy. Hydrogen segregation reduces the formation energy of defects such as vacancies, dislocations, grain boundaries, voids or crack surfaces [84]. In-situ electrochemical nanoindentation experimental results in nickel show that the activation energy for the onset of plasticity (dislocation nucleation) is reduced by dissolved hydrogen owing to the lowered shear modulus and stacking fault energy [85]. The increased compressive stress of α-vanadium micropillars (001) single crystal with increasing hydrogen concentration can be explained by the decrease in the formation energy of dislocation because hydrogen activates dislocation sources leading to an increase in dislocation density [86].

4 Experimental

4.1 Materials and sample preparation

The material used in the present study is commercial austenitic stainless steel named AISI304. The nominal chemical composition is shown in Table 4.1. The as-received samples were cold-drawn bars, and some cold-drawn rods were solution annealed at 1050 °C for 1 hour and then water quenched to obtain solution-annealed samples. Figure 4.1 showed the microstructure of cold worked and solution annealed samples. Cold working resulted in a large number of low-angle grain boundaries implying a highly deformed structure, while solution annealing eliminated a large number of defects showing annealed equiaxed grains. Low-temperature carburising treatment was carried out by Bodycote (Kolsterising® K22 process). Although the process details of the K22 process were not released due to confidential reason, it has been extensively studied by researchers [32,87]. The material conditions in this investigation are summarized in Table 4.2.

Table 4.1 The nominal composition of 304 austenitic stainless steel (wt%).

ID	C	Mn	Si	S	P	Cr	Ni	Cu	Mo	N	Fe
304	0.02	1.58	0.39	0.01	0.04	18.22	8.02	0.33	-	0.05	Bal.

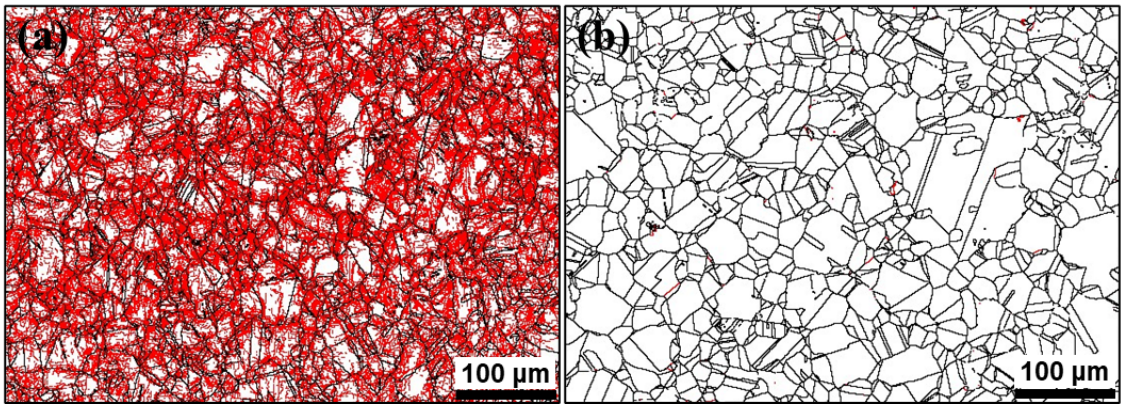

Figure 4.1 Microstructure of 304 austenitic stainless steel. (a) cold worked and (b) solution annealed. The red solid line indicates the low-angle boundary (2-15°), and the black solid line indicates the high-angle boundary (≥15°).

Table 4.2 Sample designations and their processing conditions

Name of samples	Conditions
304CW	Cold-worked 304
304SA	Solution-annealed 304
304CW-H	Cold-worked 304 charged with hydrogen
304SA-H	Solution-annealed 304 charged with hydrogen
304CW+LTC	Cold-worked 304 treated by LTC
304SA+LTC	Solution-annealed 304 treated by LTC
304CW+LTC-H	Carburized cold-worked 304 followed by hydrogen charging
304SA+LTC-H	Carburized solution-annealed 304 followed by hydrogen charging

The metallographic samples were mounted in conductive resin and plane ground with 500# SiC paper, then fine ground with 9 µm diamond suspension, followed by polishing with 3 µm and 1 µm diamond suspension and colloidal silica suspension (OPS) as the final step. To evaluate and visualize the S-phase,

V2A reagent (119 mL HCl, 12 mL HNO_3, 119 mL H_2O) was used to etch the samples for 10 s at room temperature.

4.2 Hydrogen charging

Hydrogen charging is applied to introduce hydrogen into material. Commonly used methods include gas-phase high-pressure hydrogen permeation and electrochemical cathodic hydrogen charging. The former requires complex equipment with high cost, while the latter has a simple experimental set-up with low cost and high sensitivity. In this study, hydrogen charging was performed using the electrochemical cathodic method in a solution of 0.2 mol/L H_2SO_4+ 0.01 mol/L Na_2HAsO_4. Na_2HAsO_4 acts as a hydrogen poison, inhibiting the combination of hydrogen atoms to generate hydrogen gas. For the metallographic sample, hydrogen was charged at a current density of 10 mA/cm^2 for 1-24 h at 85 °C. For corrosion and tensile specimens, hydrogen was charged at a current density of 30 mA/cm^2 for 24/72 h at 85 °C.

4.3 Characterization techniques

4.3.1 Light optical microscope

Light optical microscope (LOM) uses visible light to observe and magnify samples. It is a widely used imaging technique for various materials. The resolution of LOM is limited by the wavelength of the visible light, and it is usually possible to observe microstructures above the micrometer scale. In this work, LOM images were obtained by means of Zeiss Axioscope 7 optical microscope using ZEN core 2.7 software. The microstructure of austenitic stainless steels examined by LOM is shown in Figure 4.2. Cold working and solution annealing give different microstructures depending on the processing conditions.

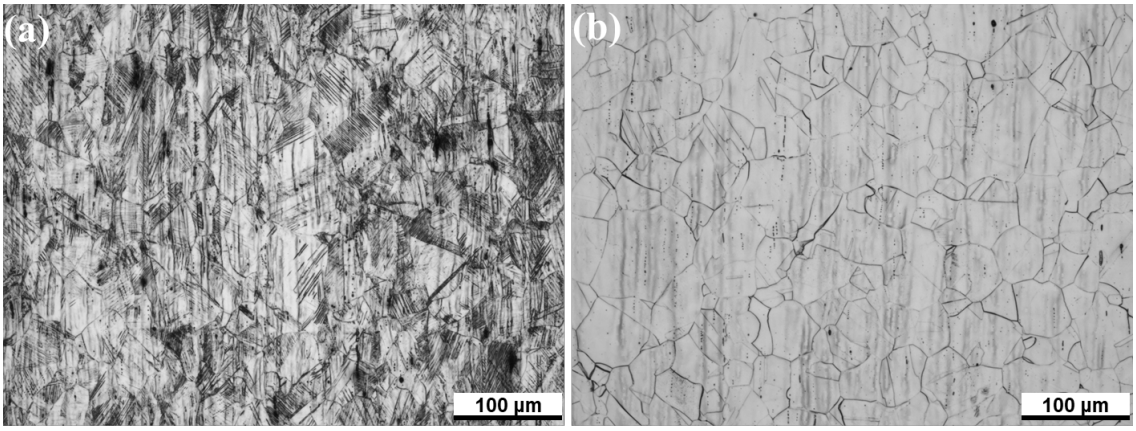

Figure 4.2 LOM shows the microstructure of austenitic stainless steels. (a) cold worked and (b) solution annealed.

4.3.2 X-ray diffraction

X-ray diffraction (XRD) produces diffraction patterns by the interaction of a monochromatic X-ray beam with electrons in the atoms of a crystal lattice. The working principle of X-ray diffraction is based on Bragg's law given in Eq. 4.1.

$$n\lambda = 2d \sin\theta \quad (4.1)$$

where n is the diffraction order, λ is the wavelength of the X-ray source, d is the diffraction interplanar spacing, and θ is the diffraction angle. XRD can be used to identify phases in materials based on crystal structure. In this study, Bruker D8 Discover with Cu-radiation source (λ = 0.154056 nm) was used with operating voltage at 40 kV and the tube current of 40 mA.

4.3.3 Scanning electron microscope

Scanning electron microscope (SEM) creates magnified images by scanning a beam of focused electrons over the surface of a sample. In SEM, the electrons emitted by the electron gun are accelerated by the electric field to the anode. The high-energy electron beam (1keV ~30 keV) is obtained and converged into an electron probe through the electromagnetic lens. When the electron probe hits the sample surface, different interactions occur between the electrons and the material, and different types of signals are emitted from the sample surface [89,90]. Typical signals (Figure 4.4) generated in electron-sample interactions include Auger electrons (AEs), secondary electrons (SEs), backscattered electrons (BSEs), characteristic X-rays and continuous X-rays.

Secondary electron signals provide important topographic information with high spatial resolution and can be used to generate morphological contrast-based images. In the most common SE mode, secondary electrons emitted by atoms excited by an electron beam are collected by a secondary electron detector (Everhart-Thornley detector). Due to the short wavelength of electrons, SEM can usually achieve a resolution of tens of nanometers. BSE electrons are deflected backwards electrons due to the interaction of electrons with the atomic nuclei of the sample. This signal has lower spatial resolution due to the large escape depth. BSE provides elemental information in the form of Z contrast (atomic number contrast). Stronger elastic scattering interactions with atoms having higher Z values produce brighter BSE images. When the electrons in the atom core shell are ejected, electrons from higher energy levels will quickly jump downward to fill the vacancy. In most cases, this transition will be accompanied by the emission of X-rays whose energy matches the energy gap between the upper and lower energy levels. X-rays have a long penetration distance, resulting in lower spatial resolution than any electronic signal. Characteristic X-rays are collected by energy dispersive spectroscopy (EDS) detectors and used to extract qualitative and quantitative chemical and compositional information from the sample. In other cases, the energy released by the downward transition is transferred to an electron in the outer shell. This electron (i.e., AE) is then ejected from the atom with an energy equal to the energy lost by the electron in the downward transition minus the binding energy of the electron ejected from the atom. AEs have very low energy, can only travel in a few atomic layers. It requires an ultra-high vacuum to reduce energy loss and sample contamination and cannot be collected in standard scanning electron microscopy.

In this work, the microstructures and fracture morphologies of the samples were examined using TESCAN MIRA4 FE-SEM and LEO Gemini 1550 FE-SEM.

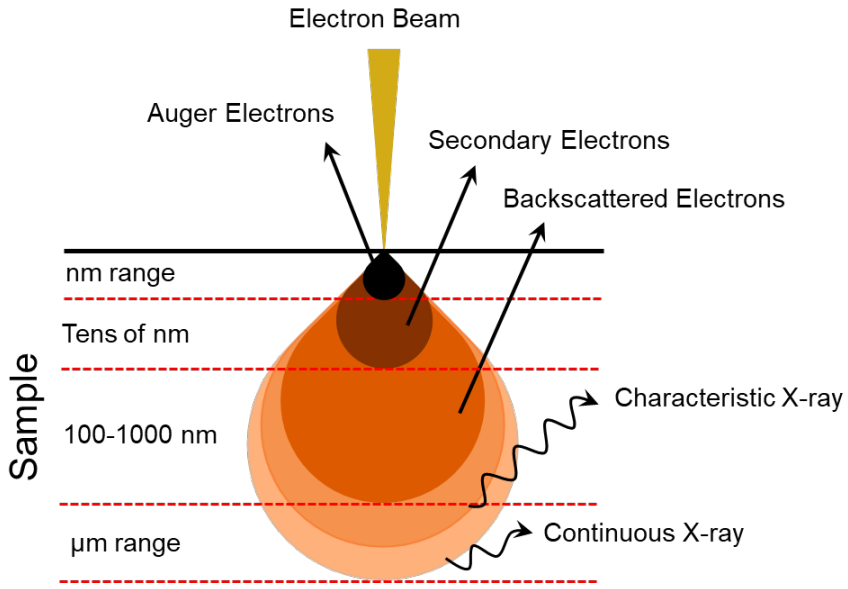

Figure 4.3 Schematic diagram of signals generated by the interaction between electron beam and sample.

4.3.4 Electron backscattered diffraction

Electron Back-Scattered Diffraction (EBSD) originated from the discovery of electron diffraction in mica sheets by Kikuchi, a Japanese scientist. Therefore, it is also called backscattered Kikuchi diffraction (BKD). EBSD is a microscopic characterization technique, which is usually assembled on the SEM to determine the orientation of the crystal regions on the surface of a large sample by automatically calibrating the backscatter diffraction pattern. EBSD detectors use high-energy diffracted electrons reflected from the sample surface to obtain a series of Kikuchi patterns. These Kikuchi patterns are generated based on Bragg diffraction and are closely related to the distance of lattice planes *d* and the crystal structure [91]. Based on database-matched crystal structure and unit cell parameters, electron backscatter patterns are indexed to provide information about the material's grain structure, grain orientation, and phases etc.

The schematic diagram of the EBSD collection is shown in Figure 4.4. In this technique, the sample is typically tilted to 70° to maximize the signal intensity reaching the detector. In the present work, EBSD was performed using an LEO Gemini 1550 FE-SEM coupled with an Oxford Nordlys collection system. The accelerating voltage was set to 20 kV, and the working distance was 14 mm. The scan step size of EBSD map acquisition was 0.3~1 μm. HKL* Channel 5 software was used for data post-processing. In this work, the maps involved include image quality (IQ), inverse pole figure (IPF), grain boundary (GB), phase and kernel average misorientation (KAM) maps. Grain boundaries with misorientation larger than 15° are superimposed as black lines in the map.

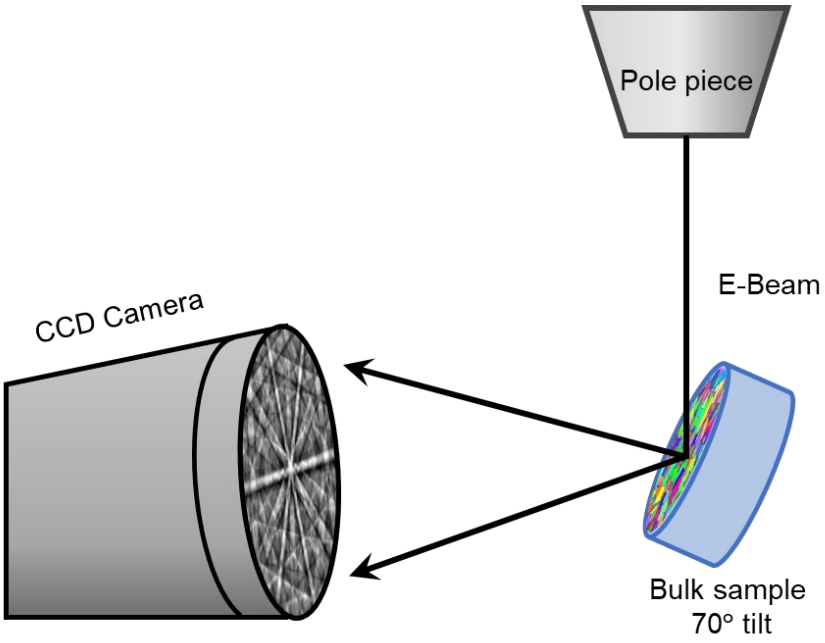

Figure 4.4 The schematic diagram of EBSD collection.

4.3.5 Electron probe micro-analyzer

Electron probe microanalyzer (EPMA) is mainly used for non-destructive chemical analysis of bulk samples. It is also known as an electron microprobe, can detect elements from Li to Pu with a detection limit of 100 ppm. The working principle of EPMA is that electron beam bombards the sample to produce diffracted electrons and X-rays. Wavelength dispersive X-ray spectroscopy (WDS) has high peak resolution and peak-to-background ratio for chemical analysis. In this study, JEOL JXA-8230 EPMA was used to determine carbon concentration as a function of depth.

4.3.6 X-ray photoelectron spectroscopy

X-ray photoelectron spectroscopy (XPS) is a surface-sensitive quantitative spectroscopy technology based on the photoelectric effect. It can identify and quantify elements and their chemical states at the surface of materials. It can also be combined with argon ion beam etching to perform depth profiling. XPS requires ultra-high vacuum ($p < 10^{-7}$ Pa) conditions. Soft X-rays with characteristic wavelengths, such as Mg K_α-1253.6eV or Al K_α-1486.6eV, are used to irradiate the surface of the sample and interact with surface atoms. Photoelectrons from different core levels of the atoms can be excited. The chemical state and content of the elements on the surface of the sample can be obtained by detecting the kinetic energy and quantity of the photoelectrons by the detector. This process can be expressed by the following formula (Eq. 4.2) [92]:

$$E_B = h\nu - E_K - \varphi \qquad (4.2)$$

where E_K is the kinetic energy of photoelectrons, $h\nu$ is the energy of incident photons, E_B is the binding energy of electrons in the sample, and φ is the work function.

When the chemical environment around an atom change, the binding energy of the photoelectrons also changes. This is called chemical shift. In this study, PHI VersaProbe III Scanning XPS microprobe (ULVAC-PHI) equipped with a monochromatic Al Kα X-ray source (hγ = 1486.6 eV) was used. The

X-ray beam size was 100 µm and take-off angle was 45°. Compositional depth profiling was performed via successive XPS analyses and Ar+ ion etching over an area of 2 × 2 mm with ion beam accelerating voltage of 2.0 kV. The nominal etch rate calibrated by using flat Ta_2O_5/Ta samples with known oxide thickness was 5.1 nm/min. The obtained spectra were analysed using Multipak software.

4.4 Mechanical and electrochemical testing

4.4.1 Hardness measurement

Hardness is a physical property of materials that reflects resistance to indentation, scratching, cutting or deformation. Hardness is generally related to strength, toughness and wear resistance. A high-hardness material is usually strong and wear-resistant but can be brittle and break easily. On the other hand, a material with a low hardness may be ductile and able to withstand deformation without breaking. There are several ways to measure the hardness of a material, the choice depends on the type of material and the required measurement accuracy. In this study, the micro-indentation Vickers hardness was applied due to the thinner carburized layer (20 - 30 µm).

Vickers hardness uses a square-based pyramidal diamond indenter with a face angle of 136°. Hardness is calculated based on ASTM E384-22 standard [93] as follows (Eq. 4.3):

$$HV = 1854.4 \times \frac{F}{d_V^2} \tag{4.3}$$

Here F is the applied force in gf and d_v is the mean diagonal length of Vickers indentation (µm). In order to reduce the accidental error of the test, the microhardness was measured on the polished cross-section from the surface of the carburized layer towards the substrate using a DuraScan 70 G5 micro-Vickers hardness tester under a load of 10 gf. The distance between the indentations follows the ASTM E92-17 standard (> 3d) to avoid interaction of deformation fields. The size of the indentation was measured by SEM, and the hardness value was averaged from five points. Figure 4.5 shows typical microhardness indentations on an SEM image.

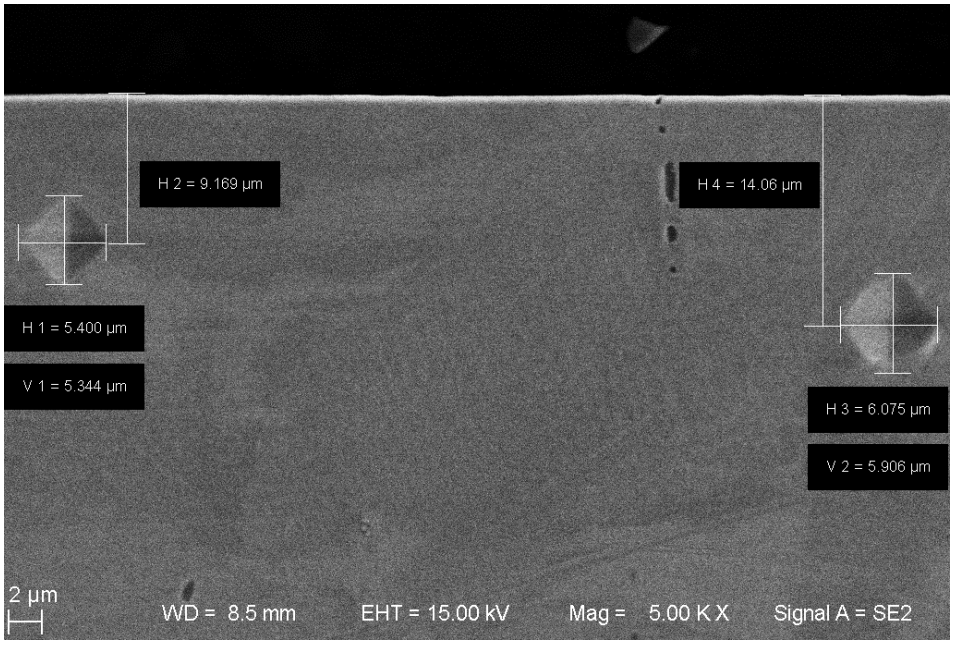

Figure 4.5 SEM image of typical microhardness indentations

4.4.2 Slow strain rate tensile testing

Tensile test specimens were prepared according to ASTM standard (E8M-22) [94] with the long axis parallel to the drawing direction. The geometric dimension is given in Figure 4.6. The samples were tensile tested using a constant slow strain-rate tensile of 1×10^{-3} s^{-1} and 5×10^{-5} s^{-1} at room temperature by means of a universal testing machine (Instron 5500R, USA). For hydrogen charged samples, the tensile test was performed immediately after charging was completed. In order to evaluate the susceptibility to hydrogen embrittlement, the hydrogen embrittlement index δ_L, or φ_L, namely relative plasticity loss, are defined in Eq. 4.3 and 4.4.

$$\delta_L = \frac{\delta_0 - \delta_H}{\delta_0} \times 100\% \quad (4.3)$$

$$\varphi_L = \frac{\varphi_0 - \varphi_H}{\varphi_0} \times 100\% \quad (4.4)$$

where δ_0 and δ_H are total elongation of uncharged and H-charged specimens, respectively. φ_0 and φ_H are area reduction of uncharged and H-charged specimens, respectively. In general, high δ_L or φ_L indicates high plasticity loss and high susceptibility to hydrogen embrittlement.

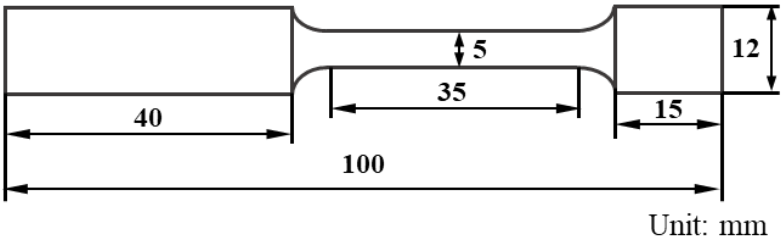

Figure 4.6 Geometries of cylindrical tensile samples

4.4.3 Electrochemical testing

In electrochemical experiments, open circuit potential (OCP) and potentiodynamic polarization tests were used for evaluating the corrosion behavior. OCP is the voltage difference between two electrodes in a system without an external circuit connection. It is an important parameter in electrochemical and corrosion behaviors because it can provide information about the corrosion resistance of materials and the electrochemical behavior of chemical reactions. The OCP test can be used to measure the corrosion potential of metals in a specific environment. Since it only provides information about the corrosion behavior of metals under static conditions, it is often used in conjunction with potentiodynamic polarization tests to gain a more complete understanding of the corrosion behavior of materials. Potentiodynamic polarization testing uses the potential-current response to determine the corrosion rate of a metal, the potential at which the corrosion rate is minimized (also known as the corrosion potential), and the passivation ability of the metal. It also determines the critical pitting potential of the metal, which is the potential at which localized corrosion, such as pitting, begins to occur. Potentiodynamic polarization testing is an effective method widely used for evaluating the corrosion behavior of metals in various environments, including aqueous, acidic, and alkaline solutions. It is commonly used in materials science and engineering to evaluate the corrosion performance of metallic coatings, surface treatments and alloys in different industrial applications.

In this study, OCP and potentiodynamic polarization tests were employed to evaluate the corrosion behavior of 304 austenitic stainless steel in 3.5% NaCl solution using a Solartron Electrochemical

Interface (SI1287). A conventional three-electrode electrochemical cell including a standard Ag/AgCl reference electrode and a platinum counter electrode was applied. The standard Ag/AgCl electrode was connected to the cell via Luggin probe. Prior to the polarisation experiments, the electrochemical cell was purged with nitrogen (5 N purity) for 60 min. The OCP test lasted for at least 2 h to reach the steady state of the system. Potentiodynamic scan started from - 0.3 V (vs. OCP) with a scan rate of 1 mV/s until the current density reached or exceeded 0.1 mA/cm^2, where breakdown potential was defined.

5 Summary of results

In this section, the results are summarized based on the appended papers. As mentioned in the **introduction**, the objective of this thesis is to evaluate the feasibility of LTC on alleviation of hydrogen embrittlement and corrosion resistance for commercial austenitic stainless steel 304. For this purpose, S-phase layer prepared by low-temperature carburizing was characterized first **(Papers I-III)**, in order to correlate the microstructure with the properties. Cathodic electrochemical method was carried out to introduce hydrogen into the samples. Paper **I** presents a preliminary study on the corrosion and mechanical properties of the S-phase after hydrogen uptake. **Paper II** focuses on the influence of LTC on hydrogen embrittlement of 304 austenitic stainless steel. **Paper III** mainly revolves around the investigation of the corrosion behavior of LTC samples after hydrogen uptake.

5.1 Characterization of S-phase

Low-temperature carburizing treatment caused changes in the microstructure and mechanical properties of the AISI 304. In terms of microstructure, LTC treatment introduced a carburized layer with a thickness of ~ 22 µm on the surface of 304, as shown in Figure 5.1a&b. The thickness of the S-phase was similar for both cold-worked and solution-annealed samples, indicating insignificant effect of processing conditions. S-phase was featureless compared to the substrate, indicating higher corrosion resistance than the substrate. The SEM image (Figure 5.1c&d) showed some randomly distributed submicron-scale pits, which may be formed due to the exfoliation of metal inclusions (sulfide/oxide) during sample preparation.

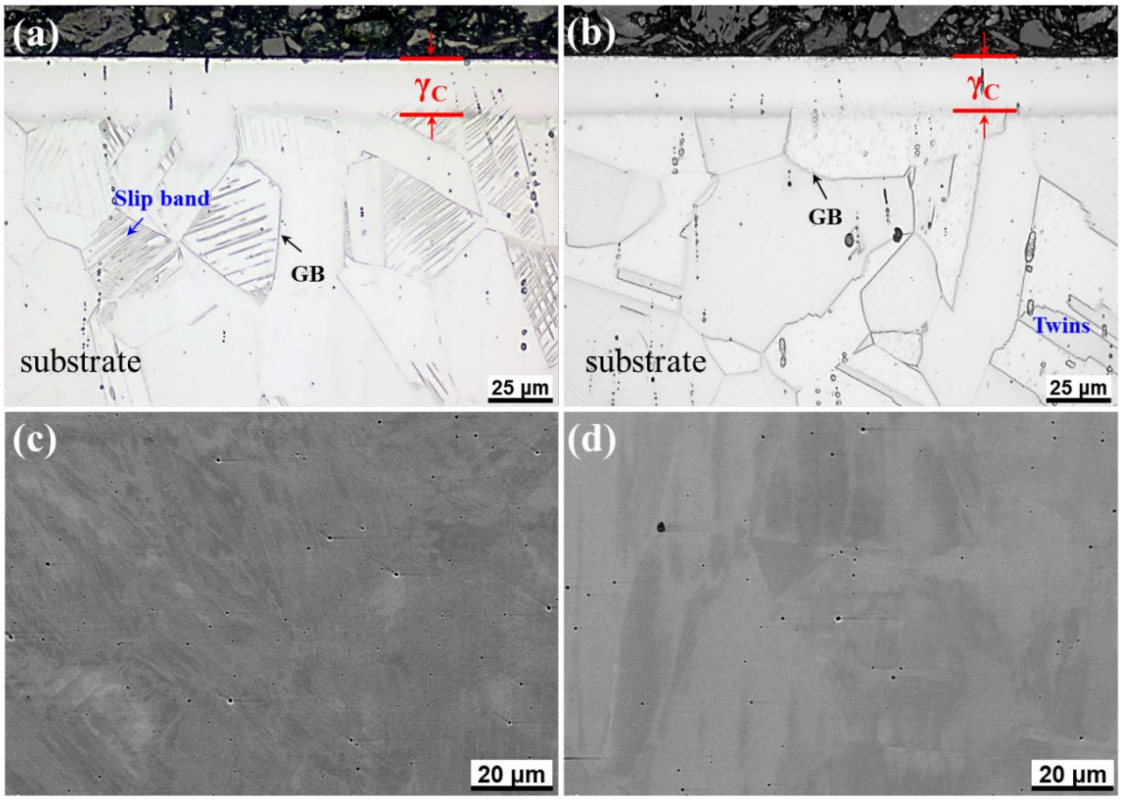

Figure 5.1 Micrographs of carburized samples: (a,c) 304 CW+LTC, (b,d) 304SA+LTC.

Carbon as an austenite stabilizing element, improves the austenite stability of metastable 304. As revealed by XRD pattern in Figure 2.5, the S-phase had a stable austenite structure compared to the

substrate containing a small amount of ferrite phase. Due to the lattice distortion caused by the solid solution of interstitial carbon, the diffraction peaks were broadened and shifted toward lower diffraction angles compared to the untreated 304. Carbon is an interstitial atom that provides solid solution strengthening effect in austenite. Therefore, carbon content has a significant impact on the mechanical properties of austenite. Carbon content and Vickers microhardness as a function of depth are shown in Figure. 5.2. The carbon concentration in the S phase (1.2 wt% for 304CW+LTC and 2.2 wt% for 304SA+LTC) is much higher than the carbon concentration in the substrate (0.02 wt%). The hardness of S-phase was also much larger than that of the substrate. Both hardness and carbon content gradually decreased with depth until reaching a stable plateau, implying that the S-phase was a diffusion-controlled continuous carburized layer. The hardness decreased with decreasing carbon concentration, confirming solid solution strengthening by interstitial carbon. The hardness of 304CW+LTCis higher than that of 304SA+LTC because cold drawing not only accumulated high-density dislocations but also triggered deformation induced martensite transformation.

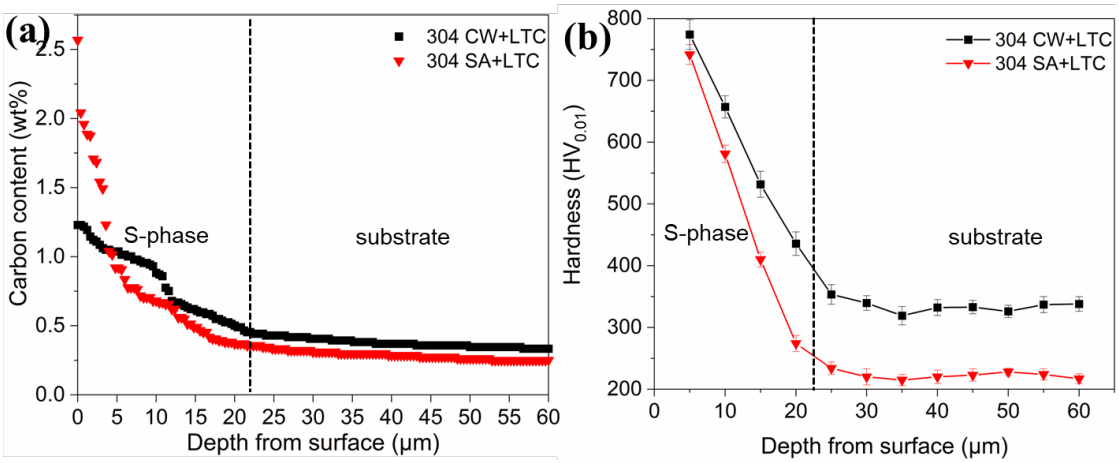

Figure 5.2 Carbon concentration (a) and Vickers hardness (b) as a function of depth for 304 LTC specimens.

5.2 Effect of hydrogen uptake on microstructure

Hydrogen enters the steel through adsorption and diffusion, causing microstructural changes. The corrosion and mechanical properties of steel are affected by the microstructure. Investigating the effects of hydrogen uptake on microstructure can reveal the mechanisms of hydrogen embrittlement and corrosion. **Paper II** described in detail that 304CW had a heavily deformed structure while 304SA showed defect-free equiaxed grains. Quasi-in situ EBSD in Figure 5.3 reveals the evolution of microstructure after hydrogen uptake. For cold-worked samples, hydrogen induced surface cracking and martensitic transformation (304CW-H). Cracks were located at grain boundaries, slip bands and voids. Martensite was observed in the original twins. Hydrogen uptake resulted in high accumulated strain of 304CW-H. 304CW+LTC-H showed stable austenite with less cracks and strains compared to 304CW-H.

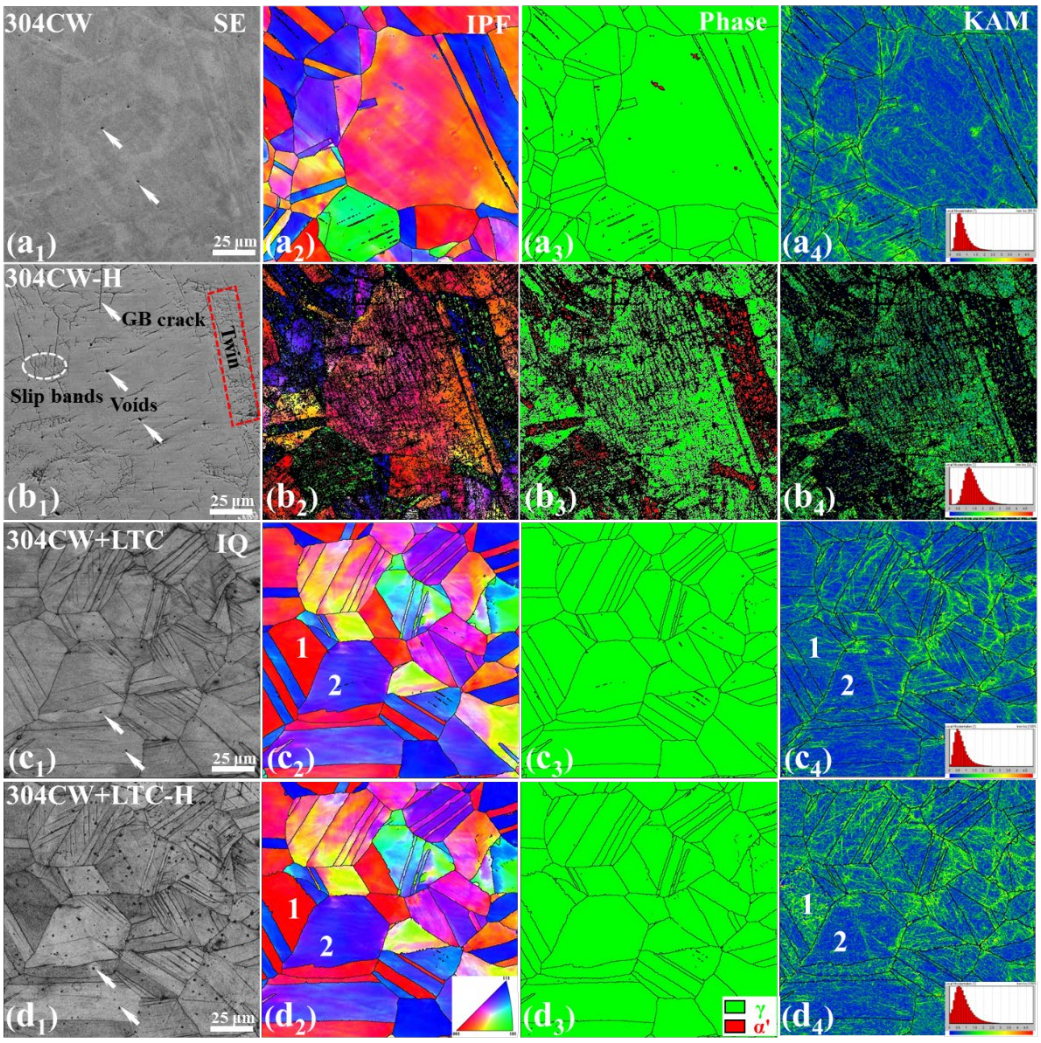

Figure 5.3 The quasi-in-situ EBSD results reveal the effect of hydrogen uptake on the microstructure. The sample was hydrogen charged at 85°C for 1 h with a current density of 30 mA/cm^2.

Hydrogen uptake may induce cracking, the extent of which varies depending on sample conditions, as revealed in Figure 5.4. The density based on crack number (ρ_{nr}) or length (ρ_l) per unit area was estimated using Image-Pro Plus and summarized in Table 5.1. The crack density in 304SA-H is less than that in 304CW-H. This can be explained by the removal of residual stress and decrease in defects from cold working by solution annealing. Compared with the 304CW-H, the crack density in the 304CW+LTC-H was significantly reduced (Table 5.1). The cracks are more tortuous as marked by the white arrows in Figure 5.4c, indicating that the LTC treatment changes the path of hydrogen-induced cracking (HIC) in austenite. However, severe delamination and fracture was observed in the 304SA+LTC-H. Compared with the 304SA-H, the 304SA+LTC-H exhibited slightly higher crack density in terms of ρ_l implying that the LTC treatment may accelerate hydrogen-induced cracking in the solution-annealed condition. The LTC samples presented smoother surfaces compared to untreated samples implying high resistance to hydrogen induced strain.

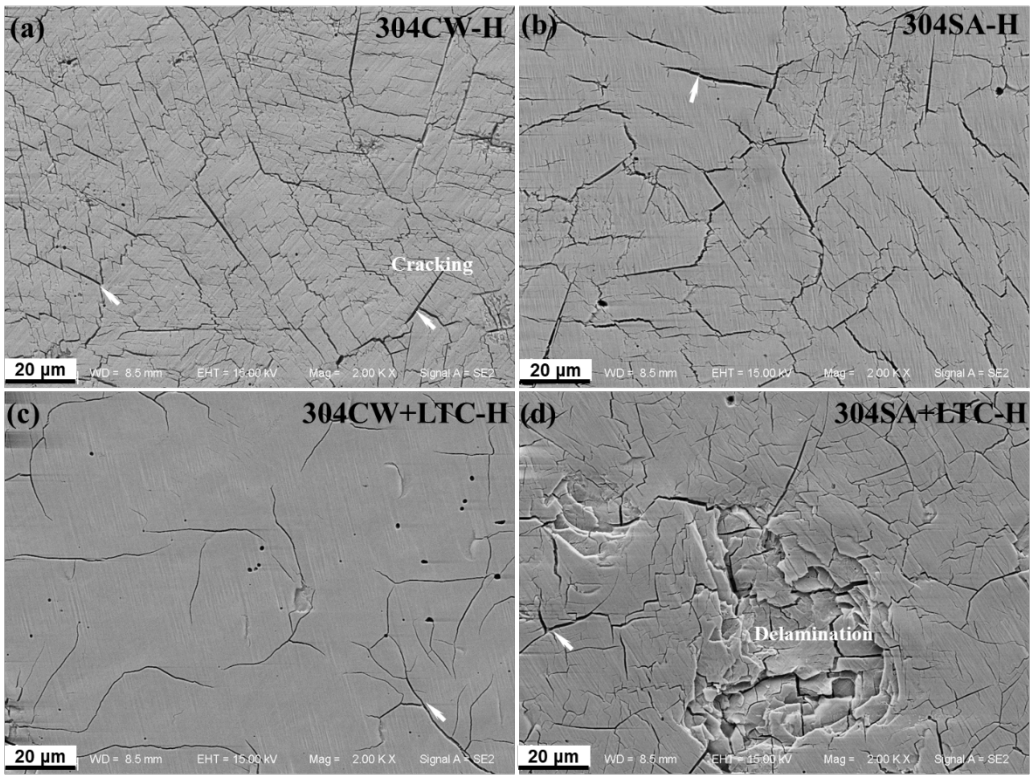

Figure 5.4 SEM images of sample surfaces in different conditions after hydrogen charging (a) 304CW-H, (b) 304SA-H, (c) 304CW+LTC-H and (d) 304SA+LTC-H.

Table 5.1 Density of cracks in AISI 304 with hydrogen uptake

Sample	304CW-H	304SA-H	304CW+LTC-H	304SA+LTC-H
ρ_l (10^4 μm mm^{-2}) *	8.8	3.5	0.8	4.2
ρ_{nr} (10^5 mm^{-2}) **	2.8	1.1	0.1	1.1

*: ρ_l is defined as the length of cracks per unit area

**: ρ_{nr} is defined as the number of cracks per unit area

5.3 Hydrogen embrittlement

Hydrogen reduces the stress in the steel for crack initiation and propagation, causing embrittlement. The most significant hazard of hydrogen embrittlement is hydrogen-induced premature fracture manifested as reduced ductility. Generally, uniaxial tensile testing was used to obtain stress-strain curves before and after hydrogen uptake to evaluate hydrogen embrittlement. **Papers I and II** used two different strain rates of 1×10^{-3}/s and 5×10^{-5}/s respectively to test the untreated and low-temperature carburized samples with and without hydrogen uptake, as shown in the Figure. 5.5. The detailed mechanical properties are listed in Table 5.2. For cold-worked samples, hydrogen uptake resulted in a significant decrease in elongation and reduction. The hydrogen embrittlement index δ_L, φ_L was significantly reduced by LTC treatment at both strain rates, indicating that low-temperature carburizing treatment improved hydrogen embrittlement resistance for cold-worked 304. Strain rate had no obvious effect on hydrogen embrittlement in this case. For solution-annealed samples, hydrogen embrittlement susceptibility decreased significantly compared to cold-worked samples. Solution annealing eliminates dislocations and martensite introduced by cold working. However, the effect of LTC on the susceptibility of solution

annealed samples was dependent on the strain rate. At a high strain rate of 1×10^{-3}/s, LTC treatment seemed to increase slightly the resistance to HE in terms of both δ_L, φ_L, but the difference was rather small. At low strain rate of 5×10^{-5}/s, LTC exhibited negative effect on hydrogen embrittlement resistance. Note that slow strain rate test allows for relatively long-term exposure to stress environments, increasing the sensitivity of the test and making it more likely to detect hydrogen embrittlement susceptibility. Hydrogen embrittlement is often associated with delayed failure, and slow strain rates allow a more accurate assessment of changes in mechanical properties over time. At slow strain rates, the order of increasing sensitivity to hydrogen embrittlement is 304SA < 304CW+LTC < 304SA+LTC < 304CW. Considering cold-worked 304 is often used for industrial applications, the result in this study has significant technical importance. LTC treatment can improve hydrogen embrittlement resistance for cold worked 304.

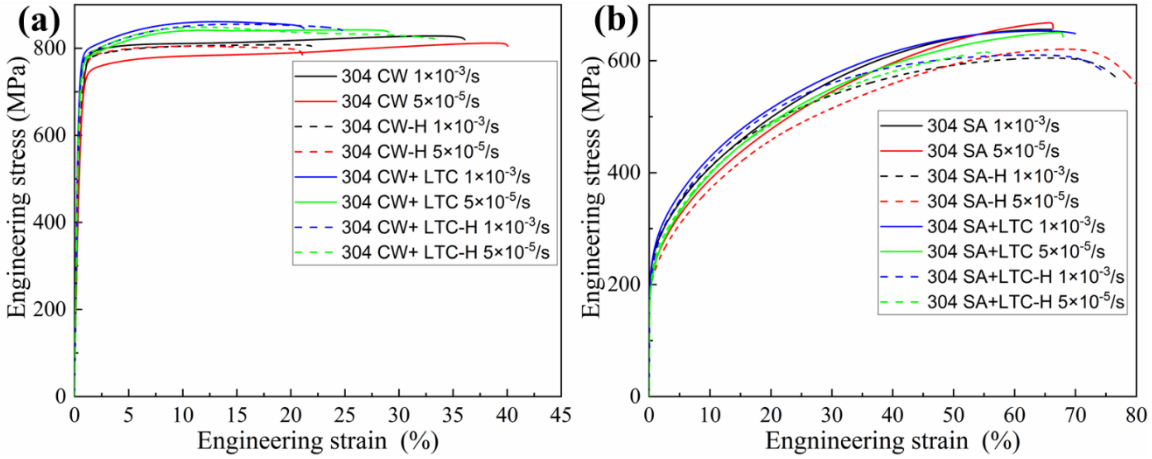

Figure 5.5 Tensile stress-strain curves of untreated and LTC treated specimens with and without hydrogen charging. (a) Cold worked condition and (b) Solution annealed condition

Table 5.2 Mechanical properties of the untreated and carburized specimens with and without hydrogen charging.

Sample	Strain rate s^{-1}	$R_{p0.2}$ (MPa)	R_m (MPa)	δ (%)	φ (%)	δ_L (%)	φ_L (%)
304 CW	1×10^{-3}	589	809	53.2	78.5	46.7	27.0
304 CW-H		581	808	28.4	57.3		
304 CW+LTC		733	861	38.8	76.5	11.9	22.0
304 CW+ LTC-H		729	855	34.2	59.7		
304 SA		216	641	75.6	82.7	9.5	12.8
304 SA-H		213	605	68.4	72.1		
304 SA+ LTC		225	655	77.8	80.0	7.5	8.9
304 SA+ LTC-H		218	610	72.0	72.9		
304 CW	5×10^{-5}	609	812	53.8	77.5	45.7	33.9
304 CW-H		692	804	29.2	51.2		
304 CW+LTC		711	842	42.4	77.0	10.4	19.6
304 CW+ LTC-H		703	848	38.0	61.9		
304 SA		200	668	72.4	77.6	5.5	13.7
304 SA-H		195	620	68.4	67.0		
304 SA+ LTC		194	651	77.2	82.6	26.9	24.6
304 SA+ LTC-H		200	616	56.4	62.3		

To further reveal hydrogen-induced fracture, fractography of H-free and H-charged samples was performed. The H-free samples showed a completely ductile fracture characteristic as demonstrated by the well-defined central dimples and surrounding shear regions throughout the whole fracture surface with prominent necking (**Papers I-II**). In H-charged conditions, as revealed in Figure 5.6, the fracture surfaces were flatter from macroscopic observation. Two different regions (Figure 5.6 a-d) with varied features were displayed, i.e., a brittle layer at the edge and a ductile region with dimples in the sample center (Figure 5.6 a_1-d_1). In addition, the final fracture area was larger than that of the H-free samples, i.e., smaller area reduction. Apparently, hydrogen uptake resulted in the premature fracture of the sample. The local high-magnification images of Figure 5.6 a_1-d_1 show shallow dimples in the H-charged samples. Cleavage fracture was observed at the edge of the fracture surface (Figure 5.6 a_2-d_2). Note that micro-void coalescence fracture was found in the center of 304SA+LTC-H (Figure 5.6d_1), while transgranular cleavage feature was found at the edges, as shown in Figure 5.6d_2. This morphology reveals that the degradation in the ductility was mainly caused by hydrogen-induced cleavage.

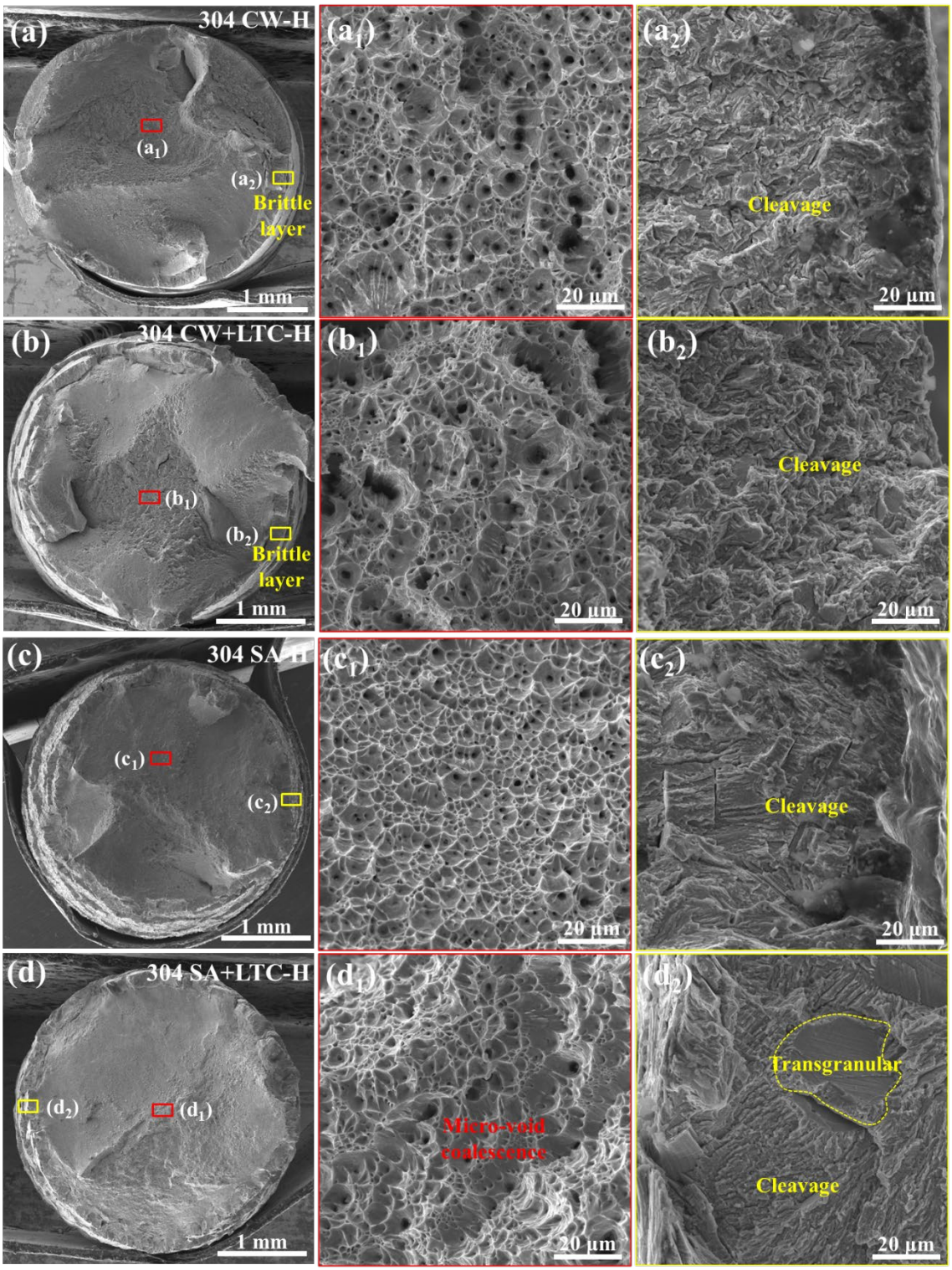

Figure 5.6 SEM fracture morphologies of samples in different conditions (a) 304CW-H, (b) 304CW+LTC-H, (c) 304SA-H and (d) 304SA+LTC-H.

To investigate the crack initiation and propagation in the hydrogen-affected zone during tensile deformation, EBSD was used. Figure 5.7 shows the microstructure on the vertical cross-section close to the edge of the fracture surface to reveal the influence of hydrogen uptake on the fracture process. The SE images showed that the crack started from the edge zone and propagated perpendicular to the tensile direction towards the center zone. A large amount of martensite α′ was observed from the cold-worked

304 charged with H (304 CW-H). Generally, martensite exhibits poor resistance to hydrogen embrittlement. Cracks preferentially propagated at α′, grain boundaries and α′/γ interfaces, which was attributed to the fact that hydrogen easily accumulated and diffused at these locations. In addition, a large number of dislocations acted as fast channels for hydrogen diffusion. The solution annealed 304 charged with H (304 SA-H) showed comparatively less martensitic phase and local strain, implying lower susceptibility to hydrogen embrittlement. For 304 CW+LTC-H, even if severe plastic deformation occurs, only a small amount of α′ remains in the matrix. Supersaturated carbon in the S-phase stabilizes austenite. The slow hydrogen diffusion in austenite increases hydrogen embrittlement resistance. However, cracks within the S-phase and low levels of strain were observed in 304SA+LTC-H. This might be related to the higher carbon concentration compared to that of 304CW+LTC, which inhibits plastic deformation leading to more brittle fracture.

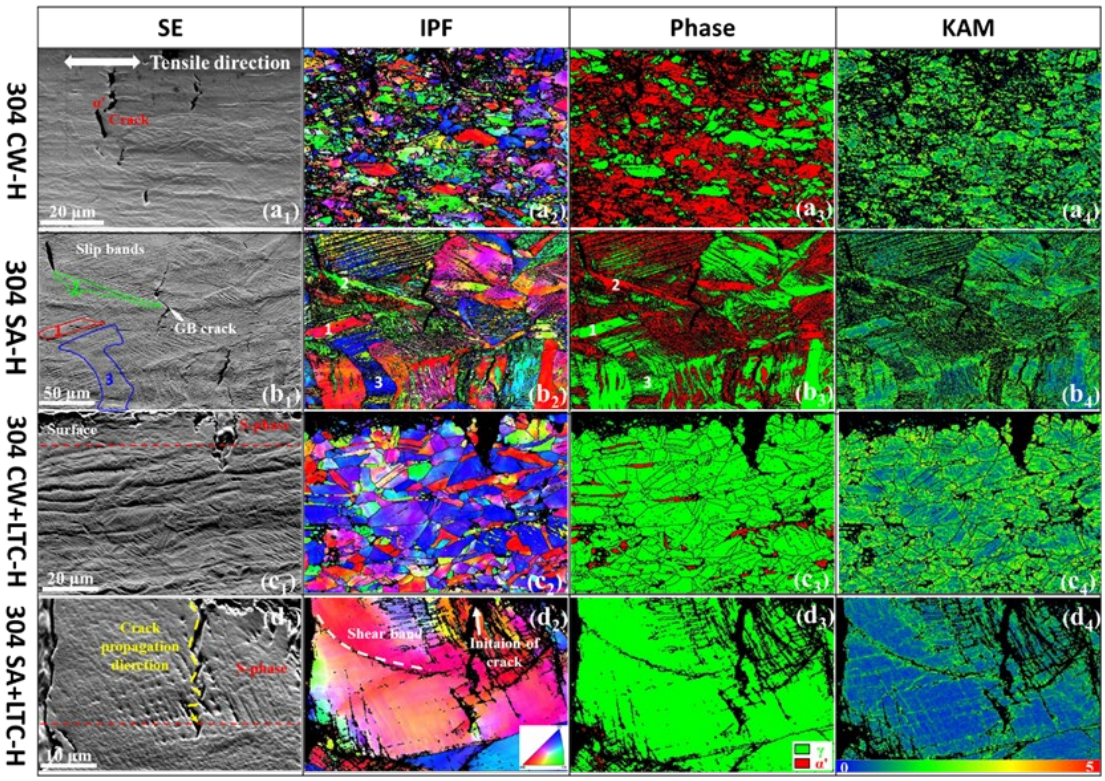

Figure 5.7 Microstructures of the H-charged samples on the vertical cross-section close to the edge of the fracture surface.

5.4 Corrosion behavior

The entry of hydrogen into steel not only causes the degradation of mechanical properties, but also the reduction of corrosion resistance of steels. The corrosion behavior of steel after hydrogen uptake is critical to its reliability.

Papers I and **III** summarized the OCP of AISI 304 in a 3.5 wt.% NaCl solution which is commonly used to simulate seawater and atmospheric environments. **Paper I** included a preliminary study on the corrosion behavior of AISI 304, so all samples were in raw conditions without polishing. However, the experimental results show that LTC treatment leads to a decrease in corrosion resistance, which is contrary to a large number of literature reports that LTC treatment improves the corrosion resistance of stainless steel. We examined the microstructure of the raw samples and found surface roughness and the presence of a small amount of carbides in the LTC samples. In order to eliminate interference, we

polished all samples to maintain the same experimental conditions. The results of **Paper III** were based on polishing all samples as conditions and inspecting the samples to ensure the same roughness and removal of extensive oxide layers and carbides. Figure 5.8(a,c) shows the open-circuit potential of the polished AISI 304 with different conditions in 3.5 wt.% NaCl solution. As expected, LTC treatment reduced OCP compared to the as-received (AR) samples, possibly due to the formation of localized carbides, which was confirmed by XRD results. However, when polished with 1 µm, the OCP of the 304 LTC was higher than 304AR. This indicates that surface conditions influence OCP. However, hydrogen caused a decrease in OCP for all samples. Qiao et al. [9] reported that the potential drop was mainly due to the dissolution of the native oxide film. LTC treatment improved the OCP of hydrogen-charging samples. The potentiodynamic polarization results also showed that hydrogen uptake decreased corrosion potential and breakdown potential. The LTC-H sample showed positive corrosion potential and breakdown potential compared to the untreated hydrogen-charged samples for both raw and polished condition. In both hydrogen-free and hydrogen-charged conditions, LTC treatment improved the hydrogen corrosion resistance potential of the surface. This beneficial effect of LTC on corrosion resistance in both hydrogen free and hydrogen presence condition was ascribed to the nobilitating effect of carbon present in the interstitial solution of S-phase. Therefore, the following section only discusses the corrosion results of polished samples (**Paper III**).

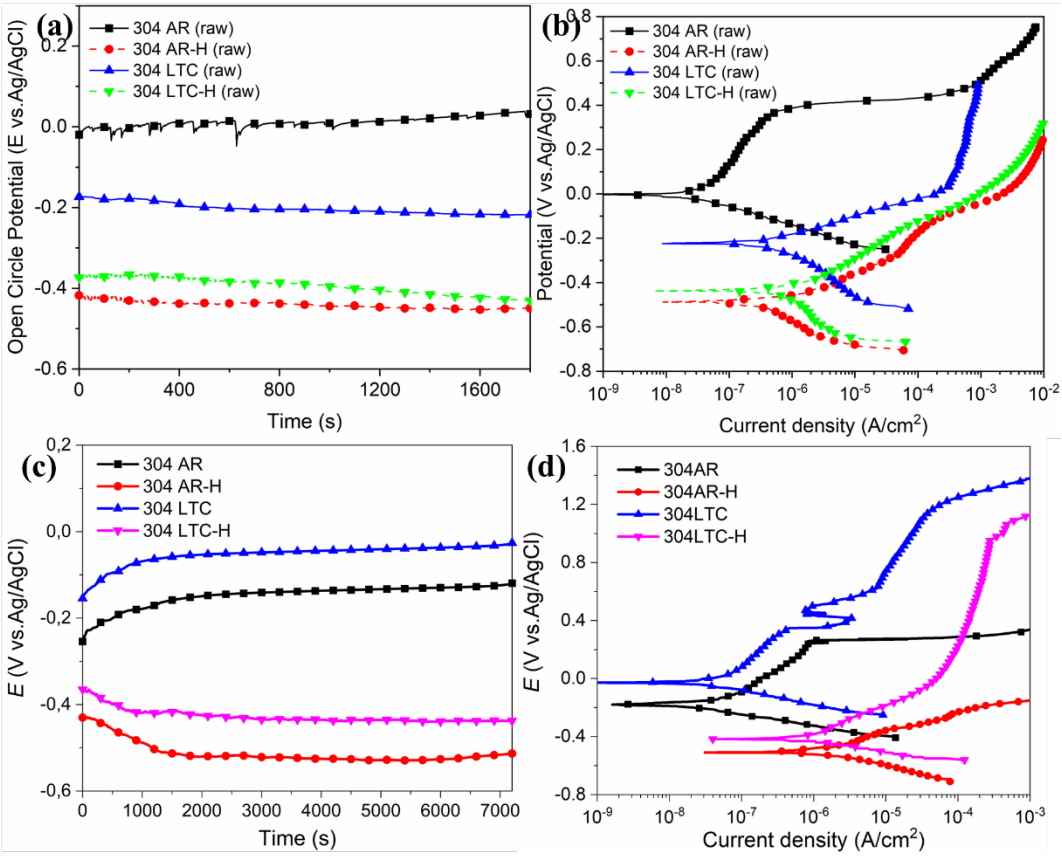

Figure 5.8 Open-circuit potential (a,c) and potentiodynamic polarization (b,d) curves of the AISI 304 with different conditions in 3.5 wt.% NaCl solution.

Figure 5.9 presents the surface morphologies of the samples with different conditions after potentiodynamic polarization in 3.5 wt.% NaCl solution. As evident from Figure 5.9a, localized corrosion pits were observed in the 304AR, but the rest of the area remained intact. The large pit caused

by the dissolution of the substrate in 304AR was 254 μm in diameter. A loose network-like film is left on the surface of corrosion pits. MnS inclusion in the substrate as shown by the blue arrow after corrosion was observed from the high-magnification images (Figure 5.9b). Inclusions, especially MnS, are known to promote initiation of pitting corrosion in stainless steels and have been extensively studied [95,96]. The surface area of 304 LTC is intact (Figure 5.9c), indicating that no severe pitting corrosion has occurred. Locally, it exhibited some very small metastable pits (~ 1 μm in size) (Figure 5.9d). For the hydrogen-charged samples (Figure 5.9e-h), severe cracking and pitting appeared on the surface after the corrosion test. At high magnification, shallow corrosion pits were found on the surface of the 304AR-H (Figure 5.9f), while the 304LTC-H showed surface cracks and delamination (Figure 5.9h). The reason may be that γ_c layer causes high local strain due to carburization as shown in Figure 2.5c, and hydrogen charging increases the internal stress causing surface cracking.

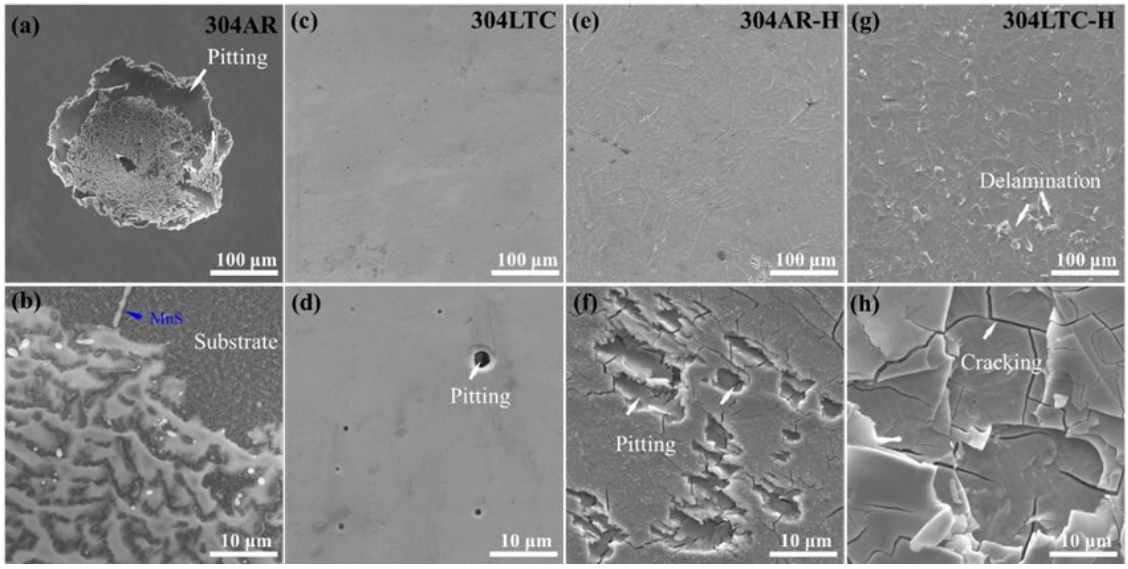

Figure 5.9 SEM images of the 304 samples after potentiodynamic polarization in 3.5 wt.% NaCl solution including (a, b) 304AR, (c, d) 304LTC, (e, f) 304AR-H and (g, h) 304LTC-H.

Figure 5.10 presents the XPS depth profiles of the main elements on the corroded surface after potentiodynamic polarization in 3.5 wt.% NaCl solution. The carbon concentration of the LTC samples (Figure 5.10b & d) in the surface region was higher than that of the untreated steel (Figure 5.10a & c) in both hydrogen-free and hydrogen-charged conditions, as expected, due to the diffusion of carbon during the treatment. LTC treatment also changed the Fe/Cr ratio in AISI 304 stainless steel after the potentiodynamic test. For 304AR, this ratio on the surface was about 1, since Cr with its strong affinity with oxygen leads to formation Cr-rich oxide layer. Below the surface, Fe/Cr ratio was close to 4, which was consistent with the nominal composition of the steel, as shown in Figure 5.10a. Low temperature carburizing modified the resulting Fe/Cr ratio at the surface (Figure 5.10b), and it was close to 2. In addition, the oxygen contents of 304AR-H were higher compared to 304AR, indicating more severe oxidation due to hydrogen uptake prior to corrosion testing. Passive film on austenitic stainless steel has been investigated extensively. In general, it is described as distinct bilayers consisting of an inner layer enriched in chromium oxide and an outer layer with a mixture of iron oxide and a hydroxide film [97-99]. Hydrogen uptake led to chromium depletion on the surface. Compared with 304AR, 304LTC showed low O content. The fast reduced oxygen concentration in the depth profile indicated a thin oxide layer in the 304LTC. Interestingly, the significantly increased carbon and oxygen content in the 304LTC-H sample resulted in relatively low Fe and Cr content compared to 304LTC. The high surface

carbon concentration caused by hydrogen uptake also caused the 304LTC-H to maintain stable austenite and brittle cracking as shown in Figures 5.3 and 5.4. The high carbon content stabilizes austenite, hinders the diffusion of hydrogen and facilitates corrosion resistance [12,44].

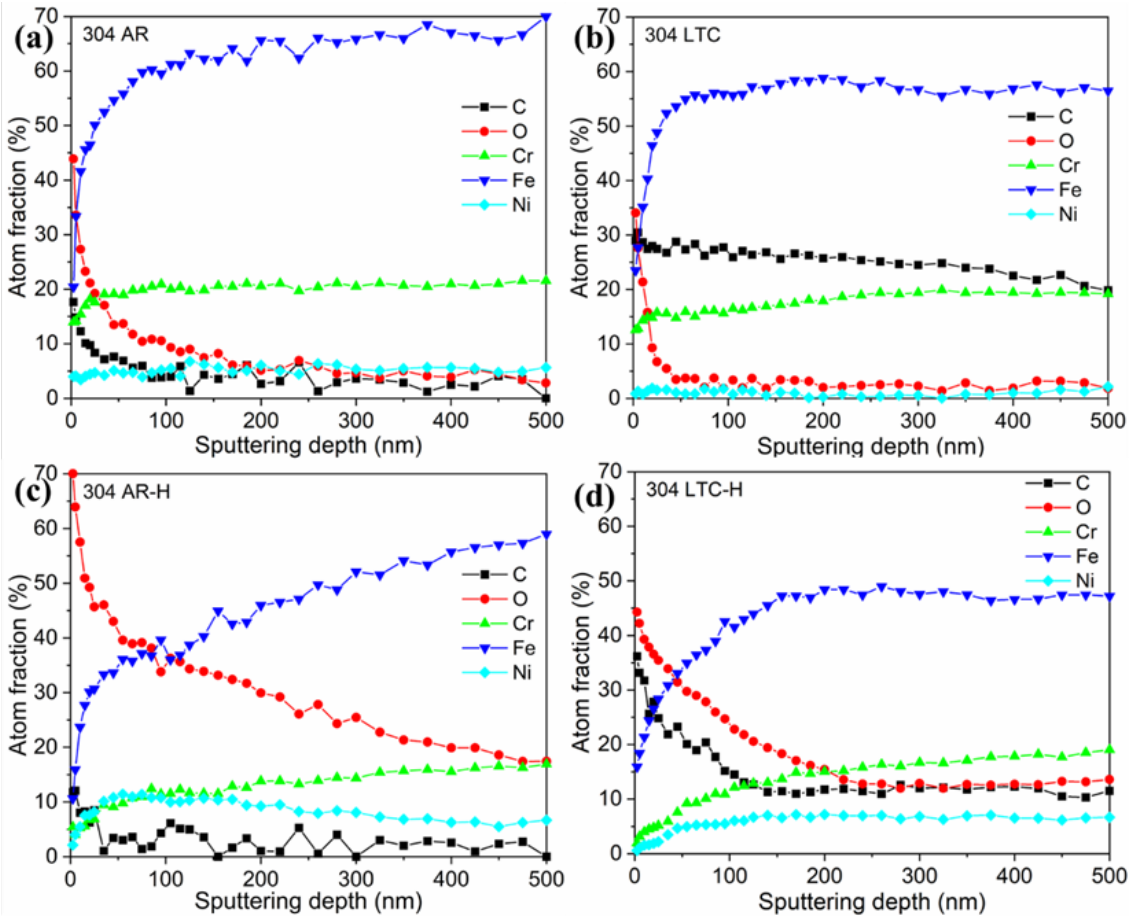

Figure 5.10 XPS depth profiles of elements in the passive films of the samples after potentiodynamic polarization in 3.5 wt.% NaCl solution. (a) 304AR, (b) 304LTC, (c) 304AR-H and (d) 304LTC-H. Etch rate is 5.1 nm/min based on Ta_2O_5 with known oxide thickness.

6 Conclusions

This work focuses on the characterization of low-temperature carburised samples with and without hydrogen uptake, and the effect of S-phase on the corrosion and mechanical properties of austenitic stainless steels after hydrogen uptake. Based on the research in this thesis, the following conclusions can be drawn:

(1) An approximately 22 μm thick S-phase is introduced into austenitic stainless steel through low-temperature carburizing. EPMA and hardness profiles indicate that the S-phase is a diffusion-controlled carburized layer. S-phase has a supersaturated carbon concentration and extremely high hardness (775 HV). The supersaturated carbon in the S phase results in a stable austenite structure and lattice distortion.

(2) All samples showed varied degrees of susceptibility to hydrogen embrittlement after hydrogen uptake. LTC treatment improves the hydrogen embrittlement resistance of cold-worked 304. The hydrogen embrittlement susceptibility of solution annealed 304 with LTC treatment was sensitive to the strain rate. At slow strain rates, the order of increased sensitivity to hydrogen embrittlement is 304SA < 304CW+LTC < 304SA+LTC < 304CW.

(3) Hydrogen-induced cracking and hydrogen-induced martensite are responsible for the high susceptibility to hydrogen embrittlement. For 304CW+LTC-H, carbon stabilized austenite inhibits martensite transformation and surface cracking to improve hydrogen embrittlement resistance. For 304SA+LTC-H, the high concentration of carbon (2.2 wt%) in the S-phase at the surface causes an increase in deformation resistance at the expense of ductility. Together with hydrogen uptake-induced cracking leads to a decrease in ductility in this case.

(4) Potentiodynamic polarization tests show that hydrogen charging reduces corrosion and pitting potential and accelerates surface corrosion of AISI 304. Hydrogen charging changed the corrosion morphology of all samples, local corrosion occurred on the surface of H-free samples, while serious pitting and cracking occurred in H-charged samples. LTC treatment improved the corrosion resistance compared to untreated samples. The carbon stabilized austenite structure inhibits martensitic transformation and improves corrosion resistance.

7 Future work

Hydrogen embrittlement and corrosion have historically been hot topics and will become more important as hydrogen energy is developing. The current work has focused on the corrosion behavior and hydrogen embrittlement of LTC treated 304 after hydrogen uptake. Considering that hydrogen content, hydrogen distribution and hydrogen diffusion are very important for systematic and in-depth investigation, we intend to explore the following directions in the future.

1. How does hydrogen content affect hydrogen embrittlement and corrosion? Is there a critical value? Thermal desorption spectroscopy (TDS) will be used to analyze hydrogen content.
2. Currently, hydrogen diffusion for stainless steels treated by LTC is rarely reported, although it is crucial to explain the hydrogen embrittlement and corrosion mechanism. Hydrogen diffusion and its kinetics warrant further investigation.
3. The distribution of hydrogen in LTC treated 304 is of interest. Using heavy water (D_2O) as a hydrogen source combined with atom probe tomography (APT) technology will help understand better the hydrogen embrittlement mechanism.
4. The current study has revealed that local strain in the grain caused by hydrogen uptake is anisotropic. Transmission electron microscopy (TEM) can be used to characterize the effect of hydrogen uptake on the dislocation density for the grains with different orientations (for example <001>, <110> and <111>-orientation). This is important for determining the controlling mechanisms behind hydrogen embrittlement.
5. The current study focuses on metastable 304 stainless steel. The hydrogen embrittlement and corrosion resistance of low-temperature carburized 316 austenitic stainless steel is also of interest.

Acknowledgements

Looking back on my two years of doctoral study, I have gained a lot. I know that I would not have been able to complete my licentiate thesis without the help and support of many people. Here, I would like to express my sincere thanks.

First and foremost, I would like to thank Prof. Emmy Yu Cao for giving me the opportunity to be her doctoral student. It is because of your support and funding that my research work is possible. Your endless care, enthusiasm, support and guidance have solved the problems I encountered. Every academic discussion with you enriches my scientific knowledge and inspires me. I am also impressed by your rigorous and scientific research attitude. You are not only my supervisor but also my friend. At the same time, I am grateful to Prof. Lars Nyborg as my examiner and Prof. Huiqing Liu as my co-supervisor, who gave me timely help when I turned to them.

Bodycote GmbH (Germany) is highly acknowledged for providing samples and low-temperature carburising treatment for this research work. I would like to thank Alexandra Bauer and Rachel Pettersson for fruitful discussions.

I would like to thank Eric Tam and Yiming Yao for their support and help in experiments and equipment training. Eric Tam gave me the instructions on electrochemical measurements and experiments. Yiming Yao helped me train metallographic sample preparation and electron microscopy. Thanks to Roger Sagdahl for helping me assemble and repair the experimental setup for hydrogen charging.

Thanks to Jessica Twedmark for helping me with my PhD admissions. I am very grateful to my office mate, James Randall and my friend Miwen Yuan for their help in my life and study. To all colleagues at the Department of Industrial and Material Science (IMS), I would like to thank you for creating an enjoyable work environment.

Last but most importantly, I would like to express my deepest gratitude and love to my family for their unselfish support and help.

Xiao Qin

Göteborg, December 2023

References

[1] G. George, H. Shaikh, "Introduction to austenitic stainless steels", In Corrosion of austenitic stainless steels, *Woodhead Publishing*, pp. 1–36, 2002.

[2] T. Michler, "Austenitic Stainless Steels", Reference Module in Materials Science and Materials Engineering, pp. 1–6, 2016.

[3] S.K. Dwivedi, M. Vishwakarma, "Hydrogen embrittlement in different materials: A review", *International Journal of Hydrogen Energy*, vol. 43 no. 46, pp. 21603–21616, 2018.

[4] T. Michler, "Toughness and hydrogen compatibility of austenitic stainless steel welds at cryogenic temperatures", *International Journal of Hydrogen Energy*, vol. 32 no. 16, pp. 4081–4088, 2007.

[5] R.A. Oriani, "Hydrogen embrittlement of steels", *Annual review of materials science*, vol. 8 no. 1, pp. 327–357, 1978.

[6] C. Zhou, Y. Song, Q. Shi, et al., "Effect of pre-strain on hydrogen embrittlement of metastable austenitic stainless steel under different hydrogen conditions", *International Journal of Hydrogen Energy*, vol. 44 no. 47, pp. 26036–26048, 2019.

[7] G. Han, J. He, S. Fukuyama, et al., "Effect of strain-induced martensite on hydrogen environment embrittlement of sensitized austenitic stainless steels at low temperatures", *Acta Materialia*, vol. 46 no. 13, pp. 4559–4570, 1998.

[8] Y. Zeng, J. Luo, P.R. Norton, "Initiation and Propagation of Pitting and Crevice Corrosion of Hydrogen-Containing Passive Films on X70 Micro-Alloyed Steel", *Electrochimica Acta*, vol. 49 no. 5, pp. 703–714, 2004.

[9] L. Qiao, J. Luo, "Hydrogen-facilitated anodic dissolution of austenitic stainless steels", *Corrosion*, vol. 54 no. 4, pp. 281–288, 1998.

[10] A. Ejaz, Z. Lu, J. Chen, et al., "The effects of hydrogen on anodic dissolution and passivation of iron in alkaline solutions", *Corrosion Science*, vol. 101, pp. 165–181, 2015.

[11] T. Bell, "Surface engineering of austenitic stainless steel", *Surface Engineering*, vol. 18, no. 6, pp. 415–422, 2002.

[12] H.K.D.H. Bhadeshia, "Prevention of hydrogen embrittlement in steels". *ISIJ international*, vol. 56, no. 1, pp. 24–36, 2016.

[13] Y. Hatano, T. Nozaki, H. Homma, M. Matsuyama, "Diffusion behaviour of hydrogen in TiC". *Annual Report of Hydrogen Isotope Research Center*, Toyama University, 2006.

[14] A.B. Belonoshko, A. Rosengren, Q. Dong, G. Hultquist, C. Leygraf, "First-principles study of hydrogen diffusion in α-Al_2O_3 and liquid alumina". *Physical review B*, vol. 69, no. 2, pp. 024302, 2004.

[15] K. Saito, S. Inayoshi, Y. Ikeda, Y. Yang, S. Tsukahara, "TiN thin film on stainless steel for extremely high vacuum material". *Journal of Vacuum Science & Technology A: Vacuum, Surfaces, and Films*, vol. 13, no. 3, pp. 556–561, 1995.

[16] T. Michler, J. Naumann, "Coatings to reduce hydrogen environment embrittlement of 304 austenitic stainless steel". *Surface and Coatings Technology*, vol. 203, no. 13, pp. 1819–1828,2009.

[17] O. Takakuwa, H. Soyama, "Suppression of hydrogen-assisted fatigue crack growth in austenitic stainless steel by cavitation peening". *International journal of hydrogen energy*, vol. 37, no. 6, pp. 5268–5276, 2012.

[18] X. Li, J. Zhang, M. Ma, X. Song, "Effect of shot peening on hydrogen embrittlement of high strength steel". *International Journal of Minerals, Metallurgy, and Materials*, vol. 23, pp. 667-675, 2016.

[19] T. Michler, "Influence of plasma nitriding on hydrogen environment embrittlement of 1.4301 austenitic stainless steel". *Surface and Coatings Technology*, vol. 202, no. 9, pp. 1688–1695, 2008.

[20] Y. Sun, X. Li, T. Bell, "Low temperature plasma carburising of austenitic stainless steels for improved wear and corrosion resistance", *Surface Engineering*, vol.15, no. 1, pp. 49–54, 1999.

[21] S.R. Collins, P.C. Williams, S.V. Marx, et al., "Low-temperature carburization of austenitic stainless steels", *ASM handbook*, vol. 4, pp. 451–460, 2014.

[22] H.M. Cobb, "The history of stainless steel", *ASM International*, 2010.

[23] J. Sun, H. Tang, C. Wang, et al., "Effects of alloying elements and microstructure on stainless steel corrosion: A review", *Steel research international*, vol. 93, no. 5, pp. 1–16, 2022.

[24] A.L. Schaeffler, "Constitution diagram for stainless steel weld metal", *Metal progress*, vol. 56 no. 11, pp. 680–689, 1949.

[25] J.R. Davis, "Stainless steels", *ASM international*, 1994.

[26] K. A. Cashell, N.R. Baddoo, "Ferritic stainless steels in structural applications", *Thin-Walled Structures*, vol. 83, pp. 169–181, 2014.

[27] R. Gunn, "Duplex stainless steels: microstructure, properties and applications", *Woodhead Publishing*, 1997.

[28] B. Weiss, R. Sticker, "Phase instabilities during high temperature exposure of 316 austenitic stainless steel", *Metallurgical and Materials Transactions B*, vol. 3, No. 4, pp. 851–866 1972.

[29] A.W. Bowen, G.M. Leak, "Solute diffusion in alpha- and gamma-Iron", *Metallurgical Transactions*, vol. 1, No. 6, pp. 1695–1700, 1970.

[30] C. Wells, R.F. Mehl, *Transactions of the Metallurgical Society of AIME*, vol. 140, pp 279, 1940.

[31] W. Batz, R.F. Mehl, C. Wells, "Diffusion coefficient of carbon in austenite", *Transactions of the Metallurgical Society of AIME*, vol. 188, pp. 553–560, 1950.

[32] O. Rey, P. Jacquot, "Kolsterising: hardening of austenitic stainless steel", *Surface engineering*, vol. 18, no. 6, pp. 412–414, 2002.

[33] T.S. Hummelshøj, T.L. Christiansen, M.A. Somers, "Lattice expansion of carbon-stabilized expanded austenite". *Scripta Materialia*, vol. 63, no. 7, pp. 761–763, 2010.

[34] T. L. Christiansen, M. A. J. Somers, "Stress and composition of carbon stabilized expanded austenite on stainless steel", *Metallurgical and Materials Transactions A*, vol. 4, no. 8, pp. 1791–1798, 2009.

[35] K.V. Werner, H.L. Che, M.K. Lei, et al., "Low temperature carburizing of stainless steels and the development of carbon expanded austenite", *HTM Journal of Heat Treatment and Materials*, vol. 77, no. 1, pp. 3–15, 2022.

[36] Y. Cao, F. Ernst, G.M. Michal, "Colossal carbon supersaturation in austenitic stainless steels carburized at low temperature", *Acta Materialia*, vol. 51, no. 14, pp. 4171–4181, 2003.

[37] Y. Cao, "Surface hardening of austenitic stainless steels via low-temperature colossal supersaturation," Doctoral dissertation, Case Western Reserve University, 2003.

[38] N. Agarwal, "Improvement of fatigue properties of stainless steel by low temperature carburization," M.S. thesis, Case Western Reserve University, 2002.

[39] J.P. Hsu, "Influence of low-temperature carburization on fatigue crack growth of austenitic stainless steel 316L", M.S. thesis, Case Western Reserve University, 2008.

[40] J. Qu, P.J. Blau, B.C. Jolly, “Tribological properties of stainless steels treated by colossal carbon supersaturation”, *Wear*, vol. 263, no. 1–6, pp. 719–726, 2007.
[41] L.J. O'Donnell, A. Heuer, G.M. Michal, et al, “Wear maps for low temperature carburized 316L austenitic stainless steel sliding against alumina”, *Surface Engineering*, vol. 26, no. 4, pp. 284–292, 2010.
[42] P. Natishan, F. Martin, A. Heuer, et al., "Enhanced corrosion resistance of stainless steel carburized at low temperature", *Metallurgical and Materials Transactions A*, vol. 40, no. 8, pp. 1805–1810, 2009.
[43] A.H Heuer, H. Kahn, F. Ernst, et al., "Enhanced corrosion resistance of interstitially hardened stainless steel: Implications of a critical passive layer thickness for breakdown", *Acta Materialia*, vol. 60, no. 2, pp.716–725, 2010.
[44] T. Li, S.C. Chien, Z. Ren, et al, "Understanding the efficacy of concentrated interstitial carbon in enhancing the pitting corrosion resistance of stainless steel". *Acta Materialia*, vol. 221, pp. 117433, 2021.
[45] F. Borgioli, E. Galvanetto, T. Bacci, "Corrosion behaviour of low temperature nitrided nickel-free, AISI 200 and AISI 300 series austenitic stainless steels in NaCl solution", *Corrosion Science*, vol. 136, pp. 352–365, 2018.
[46] J.C.P. Mignolet, "Relation between the Surface Potential and the Interaction Energy in the Case of Some Hydrogen Films", *The Journal of Chemical Physics*, vol. 23, no. 4, pp. 753–753, 1955.
[47] M. Koyama, M. Rohwerder, C. Tasan, et al., "Recent progress in microstructural hydrogen mapping in steels: quantification, kinetic analysis, and multi-scale characterisation", *Materials Science and Technology*, vol.33, no. 13, pp. 1481–1496, 2017.
[48] L.L. Shreir, Corrosion: metal/environment reactions. *Newnes*, 2013.
[49] P. Pedeferri, M. Ormellese, *Corrosion science and engineering*, Cham, Switzerland: Springer, 2018.
[50] P. R. Roberge, *Handbook of corrosion engineering*. McGraw-Hill Education, 2019.
[51] S.A. Bradford, Corrosion, *Encyclopedia of Physical Science and Technology (Third Edition)*, Academic Press, pp. 761–778, 2003.
[52] G.T. Burstein, "A hundred years of Tafel's Equation: 1905-2005". *Corrosion Science*, vol. 47, no. 12, 2858–2870, 2005.
[53] ASTM G3–14. Standard practice for conventions applicable to electrochemical measurements in corrosion testing. *Annual Book of ASTM Standards*, 2019.
[54] H. Parangusan, J. Bhadra, N. Al-Thani, "A review of passivity breakdown on metal surfaces: Influence of chloride-and sulfide-ion concentrations, temperature, and pH", Emergent Materials, vol. 4, no. 5, pp. 1187–1203, 2021.
[55] J. G. Yu, J.L. Luo, P.R. Norton, "Electrochemical investigation of the effects of hydrogen on the stability of the passive film on iron", *Electrochimica Acta*, vol. 47, no. 10, pp. 1527–1536, 2002.
[56] Q. Yang, J. L. Luo, "Effects of hydrogen on disorder of passive films and pitting susceptibility of type 310 stainless steel", *Journal of the Electrochemical Society*, vol. 148, no. 1, pp. B29, 2001.
[57] S. Thomas, N. Ott, R.F. Schaller, et al., "The effect of absorbed hydrogen on the dissolution of steel", *Heliyon*, vol. 2, no. e00209, 2016.
[58] P. He, D. Suo, W. Wu, et al., "Effects of hydrogen on the crevice corrosion behaviors of duplex stainless steel 2205", *Journal of Materials Research and Technology*, vol. 19, pp. 101–120, 2022.
[59] W.H. Johnson, "II. On some remarkable changes produced in iron and steel by the action of hydrogen and acids", *Proceedings of the Royal Society of London*, vol. 23, no. 156–163, pp. 168–179, 1875.

[60] L.B. Pfeil, "The effect of occluded hydrogen on the tensile strength of iron", *Proceedings of the Royal Society of London. Series A*, Containing Papers of a Mathematical and Physical Character, vol. 112, no.760, pp. 182–195, 1926.
[61] A.R. Troiano, "The role of hydrogen and other interstitials in the mechanical behavior of metals", *Transactions of the ASM*, vol. 52, pp. 54–81, 1960.
[62] R.A. Oriani, "A mechanistic theory of hydrogen embrittlement of steels", *Berichte der Bunsengesellschaft für physikalische Chemie*, vol. 76, no.8, pp. 848–857, 1972.
[63] C.J. McMahon Jr, "Hydrogen-induced intergranular fracture of steels", *Engineering Fracture Mechanics*, vol. 68, no. 6, pp. 773–788, 2001.
[64] W.W. Gerberich, R.A. Oriani, M.J. Lji, et al. "The necessity of both plasticity and brittleness in the fracture thresholds of iron", *Philosophical Magazine A*, vol. 63, no. 2 pp. 363–376, 1991.
[65] S.P. Lynch, "Metallographic and fractographic techniques for characterising and understanding hydrogen-assisted cracking of metals". In Gaseous hydrogen embrittlement of materials in energy technologies, Woodhead Publishing. pp. 274–346, 2012.
[66] C.D. Beachem, "A new model for hydrogen-assisted cracking (hydrogen "embrittlement")", *Metallurgical and Materials Transactions B*, vol.3, pp. 441–455, 1972.
[67] H.K. Birnbaum, S. Petros, "Hydrogen-enhanced localized plasticity—a mechanism for hydrogen-related fracture", *Materials Science and Engineering: A*, vol. 176, no. 1-2, pp. 191–202, 1994.
[68] P.J. Ferreira, I.M. Robertson, H. K. Birnbaum, "Hydrogen effects on the interaction between dislocations", *Acta Materialia*, vol. 46, no. 5, pp. 1749–1757, 1998.
[69] T. Matsumoto, J. Eastman, H.K. Birnbaum, "Direct observations of enhanced dislocation mobility due to hydrogen", *Scripta Metallurgica*, vol. 15 no. 9, pp. 1033–1037, 1981.
[70] T. Tabata, H.K. Birnbaum, "Direct observations of hydrogen enhanced crack propagation in iron", *Scripta Metallurgica*, vol. 18, no. 3, pp. 231–236, 1984.
[71] H.E. Hänninen, T.C. Lee, I.M. Robertson, H.K. Birnbaum, "In situ observations on effects of hydrogen on deformation and fracture of A533B pressure vessel steel", *Journal of materials engineering and performance*, vol. 2, pp. 807–817, 1993.
[72] S.P. Lynch, "Hydrogen embrittlement (HE) phenomena and mechanisms", *Stress Corrosion Cracking*, Woodhead Publishing, pp. 90–130, 2011.
[73] S.P. Lynch, "Environmentally assisted cracking: Overview of evidence for an adsorption-induced localised-slip process", *Acta Metallurgica*, vol. 36, no. 10, pp. 2639–2661, 1988.
[74] S.P. Lynch, "Metallographic contributions to understanding mechanisms of environmentally assisted cracking", *Metallography*, vol. 23, no. 2, pp. 147–171, 1989.
[75] S.P. Lynch, "Mechanisms of hydrogen assisted cracking–a review", Hydrogen effects on material behaviour and corrosion deformation interactions, *The Minerals. Metals & Materials Society*, Warrendale, pp. 449–466, 2003.
[76] S.P. Lynch, "Mechanisms and kinetics of environmentally assisted cracking: current status, issues, and suggestions for further work", *Metallurgical and Materials Transactions A*, vol. 44, no.3, pp. 1209–1229, 2013.
[77] M. Nagumo, "Hydrogen related failure of steels–a new aspect", *Materials Science and Technology*, vol. 20, no.8, pp. 940–950, 2004.
[78] M. Nagumo, T. Kenichi "The predominant role of strain-induced vacancies in hydrogen embrittlement of steels: Overview", *Acta Materialia*, vol.165, pp. 722–733, 2019.
[79] T. Owada, H. Suzuki, K. Takai, "Evaluation of lattice defects near hydrogen-related fracture surfaces of tempered martensitic steel", *CAMP–ISIJ*, vol. 30, pp. 851, 2017.

[80] M Nagumo, Y. Hiroshi, S. Yosuke, K. Toshiaki, "Ductile crack growth resistance in hydrogen-charged steels", *Materials Transactions*, vol. 42, no. 1, pp. 132–137, 2001.
[81] R. Kirchheim. "Reducing grain boundary, dislocation line and vacancy formation energies by solute segregation. I. Theoretical background", *Acta Materialia*, vol. 55, no.15, pp. 5129–5138, 2007.
[82] R. Kirchheim, "Reducing grain boundary, dislocation line and vacancy formation energies by solute segregation: II. Experimental evidence and consequences", *Acta Materialia*, vol.55, no. 15, pp. 5139–5148, 2007.
[83] R. Kirchheim, "Revisiting hydrogen embrittlement models and hydrogen-induced homogeneous nucleation of dislocations", *Scripta Materialia*, vol. 62, no. 2 pp. 67–70, 2010.
[84] R. Kirchheim, S. Bria, S. Petros, "Chemomechanical effects on the separation of interfaces occurring during fracture with emphasis on the hydrogen-iron and hydrogen-nickel system", *Acta Materialia*, vol. 99, pp. 87–98, 2015.
[85] A. Barnoush, V. Horst, "In situ electrochemical nanoindentation: A technique for local examination of hydrogen embrittlement", *Corrosion Science*, vol. 50, no.1, pp. 259–267, 2008.
[86] M. Deutges, I. Knorr, C. Borchers, et al. "Influence of hydrogen on the deformation morphology of vanadium (100) micropillars in the α-phase of the vanadium–hydrogen system", *Scripta Materialia*, vol. 68, no. 1, pp. 71–74, 2013.
[87] L. Ceschini, M. Carla, "Kolsterising®." *Encyclopedia of tribology*, Springer, pp. 1–14, 2013.
[88] M.A.V. Devanathan, Z. Stachurski, "The adsorption and diffusion of electrolytic hydrogen in palladium", *Proceedings of the Royal Society of London*. Series A. Mathematical and Physical Sciences, vol. 270, no. 1340, pp. 90–102, 1962.
[89] K.D. Vernon-Parry, "Scanning electron microscopy: an introduction." *III-Vs review*, vol. 13, no.4, pp. 40–44, 2000.
[90] J.I. Goldstein, D.E. Newbury, J.R. Michael, et al., *Scanning electron microscopy and X-ray microanalysis*, Springer, 2017.
[91] A.J. Schwartz, M. Kumar, B.L. Adams, *Electron backscatter diffraction in materials science*, New York: Springer, vol. 2, pp. 35–52, 2009.
[92] J. Chastain, C. Roger, J. King, "Handbook of X-ray photoelectron spectroscopy", Perkin-Elmer Corporation, 1992.
[93] ASTM E384-22, "Standard Test Method for Microindentation Hardness of Materials", ASTM international, 2022.
[94] ASTM E8M-22, "Standard Test Methods for Tension Testing of Metallic Materials", ASTM international, 2022.
[95] D. Li, F. Huang, X. Lei, Y. Jin, "Localized corrosion of 304 stainless steel triggered by embedded MnS." *Corrosion Science*, vol. 211, pp.110860, 2023.
[96] G. Wranglen, "Pitting and sulphide inclusions in steel." *Corrosion Science*, vol.14(5), pp. 331–349, 1974.
[97] C.M. Abreu, M.J. Cristóbal, R. Losada, X.R. Nóvoa, G. Pena, M.C. Pérez, "Long-term behaviour of AISI 304L passive layer in chloride containing medium", *Electrochimica Acta*, vol. 51, no. 8-9, pp. 1881–1890, 2006.
[98] R.S. Yassar, L. Scudiero, A.S. Alamr, D.F. Bahr, M.G. Norton, "Microstructure-mechanical and chemical behavior relationships in passive thin films", *Thin Solid Films*, vol. 518, no. 10, pp. 2757–2763, 2010.
[99] C.O.A. Olsson, D. Landolt, "Passive films on stainless steels − chemistry, structure and growth", *Electrochimica Acta,* vol. 48, no. 9, pp. 1093–1104, 2003.